Figure 3.6: COMSOL-modeled temperature distribution across the photocatalytic plate reactor. Due to the ease of model import between CAD programs and COMSOL, it is possible to model the temperature distribution within the stainless steel base and top plate, as well as within the quartz photo-catalyst cover, which is sandwiched between the top and bottom reactor plates.

holes for the placement of temperature control thermocouples, and four uniformly distributed blind holes parallel to the photocatalyst depression. These four blind holes were intended to be the location of standard cartridge heaters which would provide approximately 125W of thermal energy to the photocatalytic reactor base. Therefore an accurate temperature distribution model had two primary boundary conditions: heat flux input along the surface of these four holes and constant temperature on the external edges of the photocatalytic reactor.

The results of the temperature distribution studies showed that the entire catalyst bed depression should experience very uniform temperature distribution, with a variation perpendicular to the heater locations of approximately 10°C at full power. A false-color thermal image of the photocatalytic reactor operating at full heater power is shown in Figure 3.6. Note that this model was conducted with a uniform exte-

rior temperature of 300K, and the maximum catalyst temperature would be 750K. However, in actual operation, the photocatalytic reactor would be insulated with a fiberglass insulation to extend the maximum photocatalyst bed temperature to over 825K.

Gas flow distribution modeling within the photocatalyst bed was also investigated using COMSOL. The bed profile was arranged such that influent gas expanded, passed through the catalyst, then constricted as it left the modeled space. Within the simulations, the catalyst bed was modeled as a porous layer with a porosity of 0.4. This approximation allows COMSOL to treat the catalyst bed as a partially filled space, rather than a solid material, or space occupied by a fluid. Two flow cases were investigated using COMSOL. The first case was conducted with the expanding and constricting gas flow paths set to have a porosity of 1.0 (completely filled with fluid, Figure 3.7A). A line segment was chosen perpendicular to the direction of gas flow near the front and rear of the catalyst bed; the gas velocity profile was interrogated along this line for five different influent gas velocities. A second case was also investigated, wherein the expanding and constricting regions were modeled to contain porosity equal to the catalyst bed (Figure 3.7B). This case physically represents the situation where the catalyst is held in place with a packing material, either glass wool, or potentially, inert particles with the same dimensions as the photocatalyst.

3.5 Constructed Photocatalytic Reactor and Reactor Control System

Based on the SolidWorks model, a reactor was machined out of stainless steel. The reactor was heated by 4 1/4 cartridge heaters, which were controlled by LabView software. The illuminated side of the catalyst bed was sealed from the laboratory environment by a 1.0cm-thick section of GE 124 quartz (Technical Glass Products,
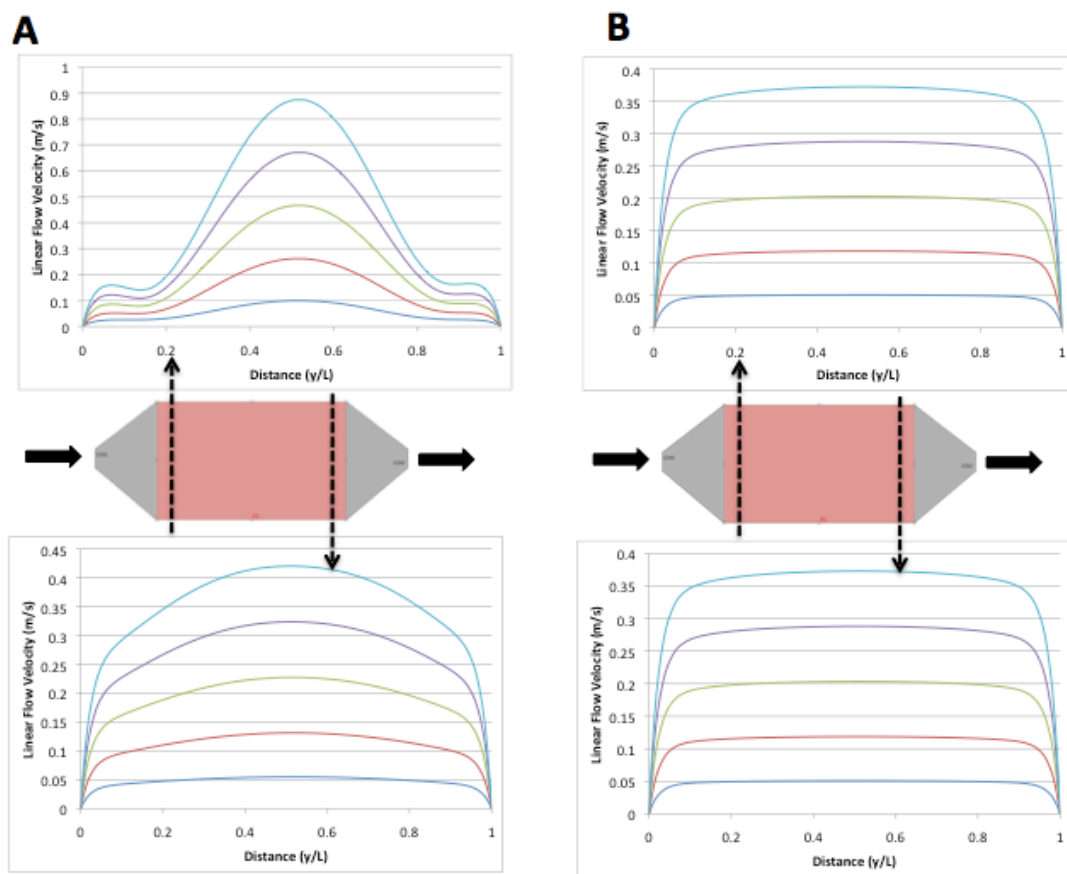
Figure 3.7: COMSOL-modeled gas flow distribution (velocity) perpendicular to the direction of flow at the inlet (top) and exit (bottom) of the catalyst bed when the model does not include (A) and includes (B) a porous gas distribution zone before and after the catalyst bed.
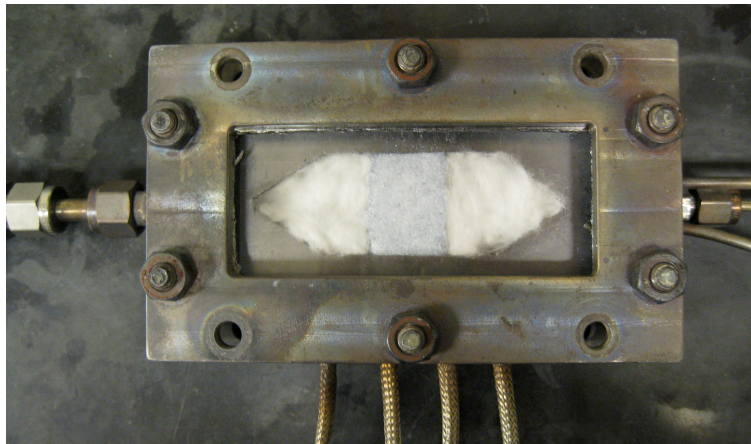
Figure 3.8: Photograph of the constructed and assembled photocatalytic reactor, filled with TiO_2 photocatalyst (center) and quartz wool packing material on either side of the photocatalyst to help retain the photocatalyst particles and to distribute gas throughout the photocatalyst bed.

90% transmission at 365nm). Quartz wool packing on the influent and effluent ends of the catalyst bed prevented channeling of the gas stream and immobilized the catalyst throughout the duration of the experiment. Figure 3.8 shows the flow reactor loaded with photocatalyst. UV illumination was achieved via a UV spot lamp (Blak-Ray B 100AP) located 10cm from the catalyst bed. Intensity measurements taken under the quartz window showed that the catalyst bed received $25mW/cm^2$ of 365nm illumination.

The photocatalytic reactor was controlled through LabView. Code was developed to record the photocatalytic reactor temperature and supply power to the 4 parallel cartridge heaters using a custom-built PID algorithm. In addition, the LabView code was set up to allow the input of an experimental control chart, which allows the user to input any required temperature steps, ramp rates, and UV lamp on/off status as a function of time. The code was also used to control a Hiden Analytical Ultra-Low Profile Mass Spectrometer. Signals recorded by LabView included: catalyst temperature, reactor edge temperature, gas flow rates from the gas mass flow controllers, lamp status (on/off), and mass spectrometer signals for masses 1 through 60.

Once the photocatalytic reactor was constructed, a temperature measurement and calibration of the reactor was required. A thermocouple was placed in the center of the photocatalyst bed, and the reactor was taken through a series of temperature steps that spanned the temperature range of interest. The results are presented in Figure 3.9.

The photocatalytic reactor temperature control program controlled the temperature of the photocatalyst bed with a linear offset relation between the set point temperature and the actual catalyst bed temperature over the temperature range of interest. In addition, it was determined that the illumination of the photocatalyst bed did not result in large temperature variations when the light was on or off. At most, the illumination caused a temperature rise of 6 °C.

3.6 Conclusions

The design, construction, and calibration of the photocatalytic reactor were done in a very methodical, informed manner. First, fluid dynamics simulations and thermal modeling were used to ensure that the proposed reactor concept would perform within expectation (uniform temperature and gas flow distribution). Once constructed, the photocatalyst temperature was measured as a function of the photocatalytic reactor set point temperature. The linear correlation between bed temperature and set point temperature allows the user to accurately control the photocatalytic reaction temperatures. With this knowledge, it is now possible to begin to measure photocatalytic rates of chemical processes.
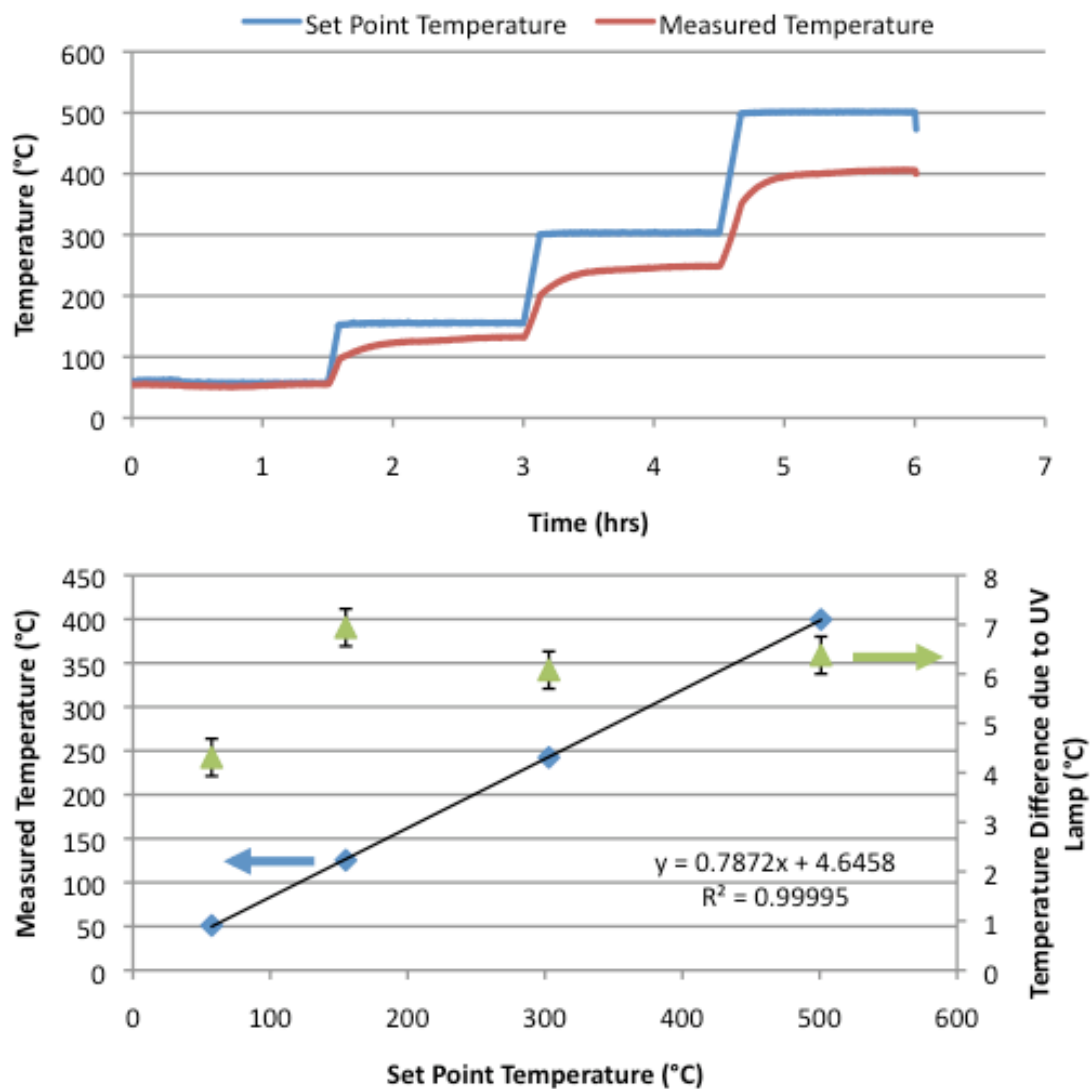
Figure 3.9: Set point temperature and photocatalyst bed temperature as a function of experiment time (Top graph), and the measured difference in temperature between set point and recorded catalyst temperature, as well as the effect of UV illumination on the photocatalyst bed temperature as a function of set point temperature (Bottom graph). All measurements were taken with the reactor externally insulated in quartz wool insulation, as it would be operated during photocatalytic rate measurement experiments.

CHAPTER IV

Photocatalytic Oxidation of Carbonaceous Deposits over TiO$_2$

4.1 Abstract

This work is the progression of the coal gasification work conducted during the preliminary investigation of this thesis. As the major impediment toward the observation of high temperature photocatalytic gasification reaction rate measurements was the ability to introduce ultra-violet photons into the catalyst bed, this work was re-addressed upon the completion of the photocatalytic reactor.

The rates of photocatalytic removal of carbonaceous species deposited on TiO$_2$ were measured at photocatalyst temperatures of 40 °C and 200 °C, respectively. Raman data revealed that the ratio of carbonaceous species to TiO$_2$ decreased with increasing time on stream, and the rate of photocatalytic oxidation increased with catalyst temperature. Infrared spectroscopy revealed that photocatalytic oxidation occurs via a loss of terminal Ti-OH hydroxyl species. At elevated temperatures, the photocatalyst surface became partially deactivated by the accumulation of reaction intermediates, such as carboxyl groups with increasing time on stream; while the concentration of surface hydroxyl species remained constant. However, Raman data suggested that the graphitic carbon crystallite size continued to decrease after the

catalyst was partially deactivated. This indicates that carbon oxidation continued even after loss of photocatalytic activity, presumably via an O_2-superanion. Additional experiments explored the role of water on photocatalytic oxidation reactions and results are briefly discussed.

4.2 Introduction

In general, catalyst deactivation and poisoning (e.g. carbon deposition and sulfur poisoning) are two primary limitations to catalyst lifetime and efficiency [37, 85, 86]. Currently, catalyst regeneration or replacement is required to improve the performance of deactivated catalysts. However, in many cases, catalyst regeneration only partially restores the diminished activity of the catalyst. For example, regeneration of carbon-deactivated catalysts typically involves an oxidative regeneration procedure, which can produce very high catalyst temperatures during the exothermic oxidation of deposited carbon. Such high temperatures during regeneration promote catalyst sintering, which can permanently reduce active catalyst surface area and leads to diminished activity [85, 86]. Typically, a substantial amount of thermal energy is required to raise the catalyst temperature to initiate regeneration. In some cases, the deactivated catalyst bed must reach temperatures in excess of 500 °C before carbon deposits can be removed [37]. Therefore, novel photocatalytic oxidative regeneration procedures would be highly desirable and could potentially operate at lower temperatures, thereby avoiding process downtime and operational inefficiencies if such regeneration processes could be effectively conducted between 100 °C < T < 400 °C. Specifically, such procedures should leverage photo-generated electronic energy (via incident solar energy) against the Arrhenius effects of increasing temperature on reaction rate (such as carbon oxidation rate, in the present example). Indeed, increased catalytic rates of reaction have been recently observed using a combined photo-thermal approach (on the order of 3-8 times) for semiconductor oxidation pho-

tocatalysis and metal nanoparticle-based plasmon epoxidation catalysis [2, 87].

Photocatalytic oxidation over bare semiconductors has been shown to effectively oxidize organic compounds, such as aromatics, alkanes, alkenes, alcohols, and even soot [9, 88–91]. Semiconductor-based oxidation mechanisms typically proceed in this order: 1) Photo-generated holes oxidize surface-terminal hydroxyl groups to form radicals, 2) Hydroxyl radicals react with adsorbed carbon chains, which then form reactive carbonyl and formate groups, or mineral acids, and 3) Adsorbed mineral acids further decompose into CO_2 and H_2O. Some research has shown that carbonaceous material deposited on TiO_2 can be photocatalytically oxidized through the aforementioned mechanism [9, 91]. Although the observed rate of carbon oxidation is very low, it might be possible to utilize a photo-thermal oxidation route to accelerate the observed oxidation rate of carbonaceous species by introducing additional thermal energy to overcome kinetic reaction barriers.

Here, we describes a photo-thermal oxidation of carbonaceous species deposited on bare TiO_2. The aim of this work is to explore the feasibility of using elevated temperature photocatalysis to enhance the observed reaction rates of processes that are currently driven photocatalytically. In addition, this paper shows that, through a photo-thermal process driven at moderate temperatures (i.e., temperatures below those required to thermally oxidize species), it is possible to increase the rate of oxidation of relatively stable compounds (such as graphitic carbon). The use of a novel photocatalytic reaction vessel provides a large exposed gross catalyst bed area for both ultra-violet illumination and Raman spectroscopic surface characterization of carbonaceous species. Evidence of reaction intermediates was observed using diffuse reflectance infrared spectroscopy.

4.3 Experimental

Titania used in this study was synthesized via a sol-gel process using titanium butoxide (TBO, Sigma-Aldrich #244112). A 1:1 mixture of DI water and ethanol was first stirred for 30 minutes at room temperature; the pH of the solution was adjusted to 1.0 with hydrochloric acid and allowed to stir for an additional 30 minutes. TBO was mixed with an equal volume of ethanol and added drop-wise into the ethanol/water mixture. After each addition, the solution became momentarily turbid before becoming clear again. After TBO addition, the mixture was allowed to stir for 3 hours at room temperature. The solution was then refluxed at 80 °C for 18 hours to condense TiO_2. The resulting gel was centrifuged to remove excess water and ethanol, then dried at 120 °C overnight. The dried TiO_2 was calcined at 500 °C in air for 5 hours to remove any remaining butanol precursors and then ground to 80-120 mesh.

The recovered TiO_2 particles were physically mixed with hydroxyethyl cellulose (Sigma-Aldrich #09368) to a 20wt% ratio of cellulose. DI water was added to wet all of the catalyst mixture, which was then placed in an ultrasonic bath for 1 hour. The slurry was then allowed to dry at 120 °C overnight. The cellulose-coated TiO_2 was then pyrolyzed in a furnace in nitrogen at 300 °C for 1 hour. Thermogravimetric analysis on cellulose-coated TiO_2 revealed that the cellulose completely decomposed to stable carbon species at 250 °C in nitrogen. The resulting carbon-modified TiO_2 was then ready for photocatalytic oxidation experiments.

The photocatalytic oxidation experiments were conducted in a specially designed reactor with a flat catalyst bed (described elsewhere [2]). Approximately 200mg of carbon-modified TiO_2 was placed in the reactor, which was then heated to reaction temperature. A water aerator was used at 20 °C to humidify dry air; this wet air stream was introduced to the reactor. A Black-Ray UV lamp delivered 25mW cm^{-2} of 365nm light to the catalyst bed, which was approximately 5cm x 5cm on edge. The

photocatalytic oxidation experiment was conducted for 12 or 48 hours at 40 °C or 200 °C, respectively. A set of control experiments without UV irradiation was conducted at 200 °C. This temperature is lower than the thermal oxidation temperature of the carbon modified TiO_2 (approximately 375 °C in air atmosphere).

Post-reaction sample characterization was conducted using Raman spectroscopy. Given the nature of the photocatalytic reaction vessel, in situ spectroscopic experiments allowed precise investigation of surface species in the carbon-modified bed. Nine spatially distributed Raman measurements were taken over the surface of the catalyst bed. Post-processing of the spectra was conducted in Matlab; removal of background fluorescence was required for all samples, however, samples exposed to extended time periods of UV irradiation appeared to have more fluorescence than other samples, making post-processing difficult. Gaussian fitting of the E_g peak of TiO_2 (143 cm^{-1}) and the G and V_R carbon peaks [90] was also conducted in Matlab.

Diffuse Reflectance Infrared Spectroscopy (DRIFTS) was used to characterize oxidation intermediate species produced during the initial 1 hour of reaction on fresh carbon-modified TiO_2. Carbon-modified TiO_2 was mixed with KBr to 6wt%, ground, then introduced to the DRIFTS sample chamber. Dry air was passed through the sample chamber, while the sample was heated to 120 °C for 30 minutes to remove physisorbed water. The sample was then cooled to 40 °C before IR spectra were recorded. The first spectrum was recorded in the absence of UV light; this spectrum was used as a background for comparison with spectra taken during UV illumination. Spectra were recorded using 512 scans with 4cm^{-1} resolution. Spectra were recorded at 15-minute intervals beginning immediately after onset of UV illumination.

4.4   Results and Discussion

Figure 4.1 shows photographs of the carbon-modified TiO_2 in situ after photocatalytic oxidation. The surface of the catalyst was markedly lighter after photocatalytic
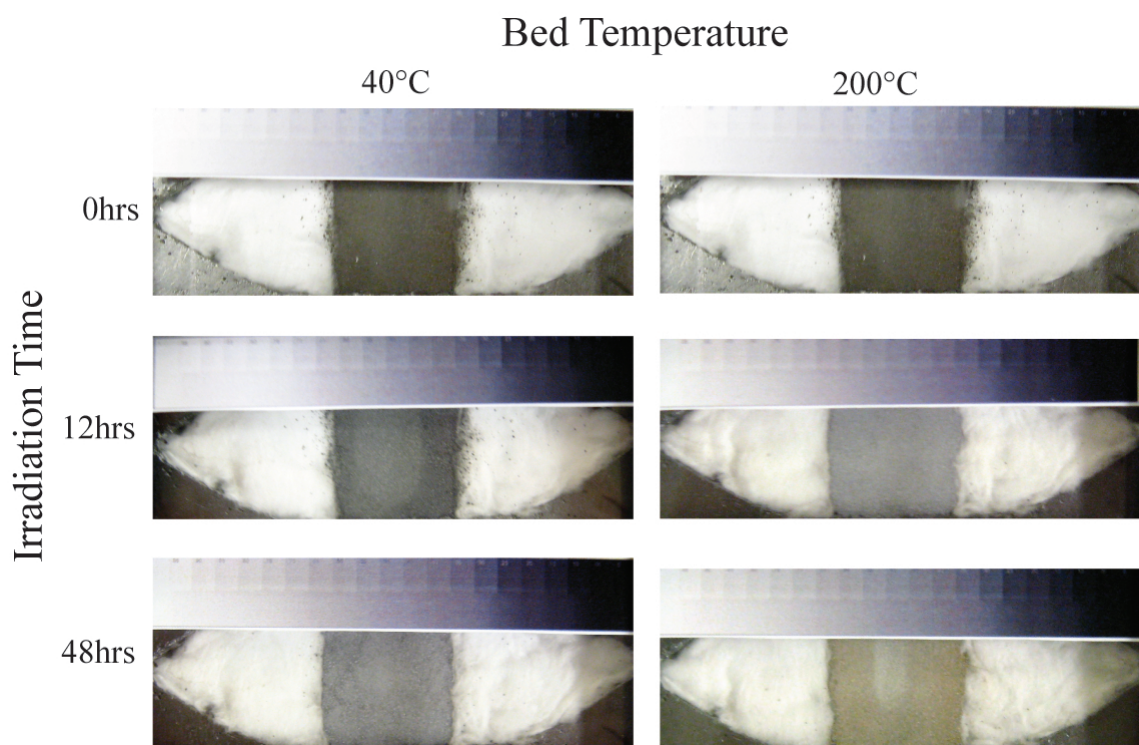
Figure 4.1: Images of carbon-modified TiO_2 beds in situ after photocatalytic reaction at 40 or 200 °C and 0, 12, or 48 hours. One grayscale color indicator was used in all photographs to aid in visual comparison between different samples.

oxidation, supporting results presented previously [9, 91]. Manual catalyst bed profiling reveals that the effects of photocatalytic oxidation were limited to a depth of approximately 50μ; it is believed that, due to the small catalyst particles, packing fraction and absorption properties of the catalyst bed, transmission of UV photons further into the catalyst bed is limiting. Therefore, oxidized carbon was mainly localized to regions close to the catalyst surface that was irradiated with UV light. Removal of the catalyst bed for characterization (e.g. thermogravimetric analysis) averages the effects of reaction over the entire catalyst bed, thereby limiting the inherent ability to observe changes in carbon content due to photocatalytic oxidation. This prompted us to conduct in-situ surface characterization of the carbon-modified TiO_2 using Raman spectroscopy, as this allows for the characterization of carbon and TiO_2 species exposed to oxidation. Figure 4.2 illustrates representative Raman spectra for the give experimental conditions; these spectra have been corrected for background fluorescence. The sinusoidal noise observed in oxidation samples from 48 hours of illumination at 40 °C and 12 and 48 hours of illumination at 200 °C results from the Raman spectrometer used. At low signal intensities (i.e. long oxidation times or high oxidation temperatures), this noise becomes large in relation to the observed TiO_2 or carbon signals. Raman results presented in Figure 4.2 illustrate two interesting results: the decrease in peak intensities for carbonaceous species with respect to the TiO_2 peak at $143cm^{-1}$, and the decrease of the carbon G band with respect to the carbon V_R band only at elevated photocatalyst temperatures. These two effects were quantified using Gaussian fitting of known carbonaceous Raman features.

Gaussian fitting of several Raman-active carbon modes (listed in reference [90]) resulted in the precise fitting of the carbonaceous peaks observed between 1400 and $1700cm^{-1}$. The V_R and G carbon features are of specific interest in this study, as they are due to amorphous and graphitic carbon structures, respectively. The
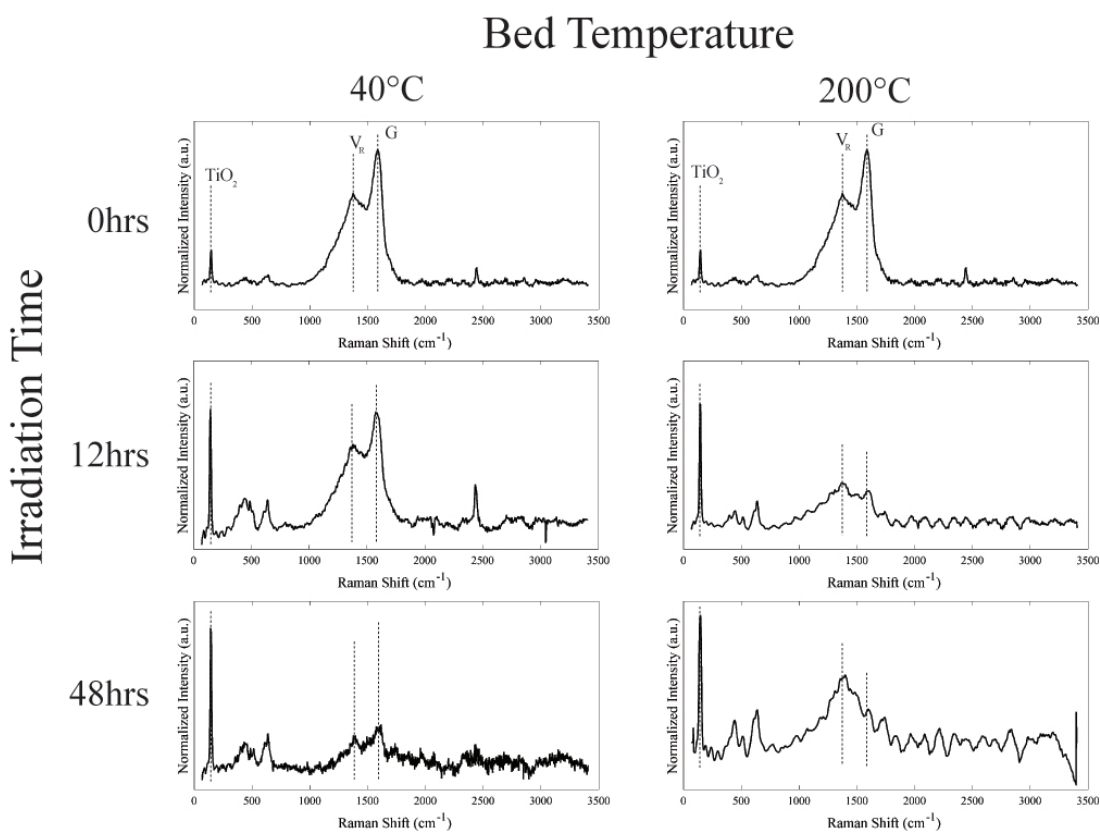
Figure 4.2: Raman spectra of carbon-modified TiO_2 for each reaction condition. (fluorescence corrected) Although nine spectra were recorded for each sample, only one is shown here. Dotted lines are used to show the Eg vibration of TiO_2 and the V_R and G vibrations of carbon. Spectra from 40 °C/48hrs, and 200 °C/12 and 48hrs show significant sinusoidal noise which resulted from original Raman data collection.

E_g TiO$_2$ feature at 143cm^{-1} was also fit using a Gaussian function. The resulting TiO$_2$ peak area was compared to the sum peak area of carbonaceous features; this ratio was used as a qualitative measure of surface carbon coverage (Figure 4.3A) and supports the visual observations of relative carbon coverage in Figure 4.1. The FWHM of V_R and G carbon peaks are shown in Figure 4.3B and Figure 4.3C. Raman peak widths have previously been correlated to crystallite size and graphitic order in carbon-containing samples [92, 93]. The effect of increased photocatalyst temperature appears to accelerate the photocatalytic oxidation process, as observed by the slope of the carbon-titania ratio as a function of illumination time (Figure 4.3A).

As measured by Raman spectroscopy, the Raman band-width of the amorphous carbon structures present on the post-reaction samples (Figure 4.3B) do not vary significantly over the course of a 48-hour experiment for either reaction temperature studied. However, when compared against the 200 °C thermal oxidation control experiment, the presence of UV-illumination appears to remove some amorphous species. Raman band-width results from the graphitic carbon structures are more conclusive (Figure 4.3C). At low reaction temperatures (40 °C), the graphitic crystallite size remains relatively constant over a 48-hour reaction period, while at high reaction temperatures (200 °C), this decreases dramatically over the course of the 48-hour experiment. This result suggests that increased reaction temperatures are necessary to overcome the kinetic barrier for the removal of graphitic carbon structures through a photocatalyzed oxidation mechanism. Detailed mechanistic and chemical intermediate information can be gained from DRIFTS observation of the photocatalytic oxidation reaction at both reaction temperatures.

DRIFTS results from the photocatalytic oxidation of carbon-modified TiO$_2$ at 40 °C (Figure 4.4) reveal interesting transient information on the state of the catalyst. The largest observed changes in absorbance relate to the decreased presence of hydroxyl compounds, as evidenced by the features at 3493 and 1635 cm^{-1}. This ob-
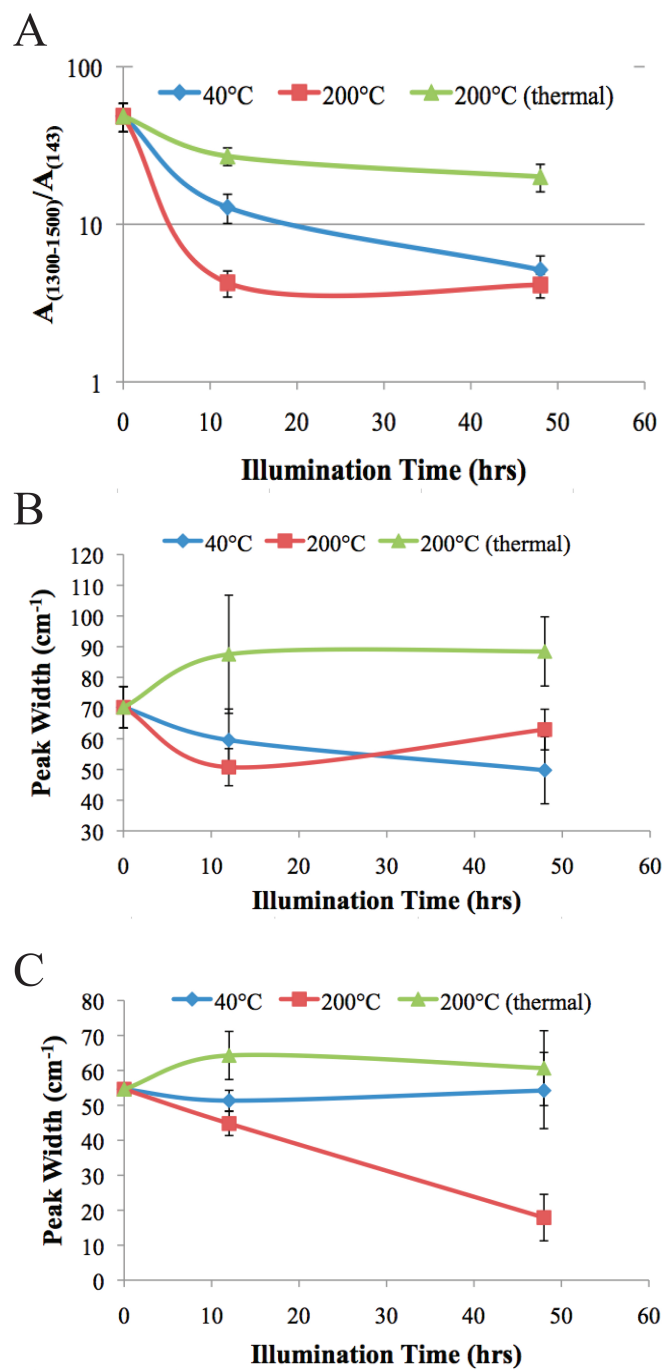
Figure 4.3: Results from Gaussian fitting of Raman spectra for the ratio of TiO_2 to carbon-species (A), the FWHM of the VR carbon peak at $1390cm^{-1}$, which is associated with amorphous carbon structures (B), and the FWHM of the G carbon peak at $1590cm^{-1}$, which is associated with graphitic carbon structures (C). Error bars denote the 90% confidence interval, as calculated from the 9 Raman spectra taken per sample.
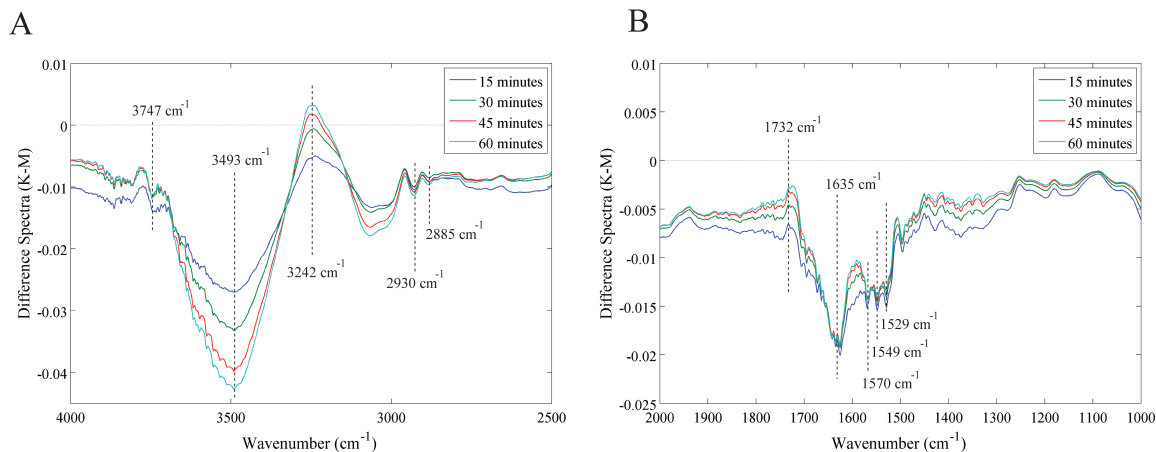
A   B

Figure 4.4: DRIFTS difference spectra (Kubelka-Monk units) of UV-illuminated carbon-modified TiO_2 at 15-minute intervals during the first 1 hour of photocatalytic oxidation at 40 °C. The background used to acquire these samples was the dry carbon-modified TiO_2 sample immediately prior to UV illumination.

servation is consistent with previously published results in which decreased hydroxyl concentrations are observed during the photocatalytic oxidation of hydrocarbons such as propane and acetone [94–96]. In addition, several features between 1570 and 1529 cm^{-1} and features at $2930cm^{-1}$ and $2885cm^{-1}$ are observed to immediately decrease upon UV irradiation. These stretching frequencies correspond to the asymmetric and symmetric stretching frequencies of formate species [88]. These features are observed prior to UV-illumination and are hypothesized to be a result of incomplete pyrolyzation of the carbon precursor. In addition, the feature at $3747cm^{-1}$ is observed to decrease upon illumination with UV light; this feature can be attributed to terminal hydroxyl groups on Ti(IV)-OH [89, 94, 96, 97].

In contrast, features at 3242 and 1732 cm^{-1} were observed to increase over the course of the 60-minute DRIFTS experiment. These features have been associated with formic acid that is hydrogen-bonded to the TiO_2 surface [94]. Meulen, et al. observed the production of formic acid and a decrease in hydroxyl groups during the photocatalytic oxidation of propane over anatase and rutile TiO_2 in a DRIFTS
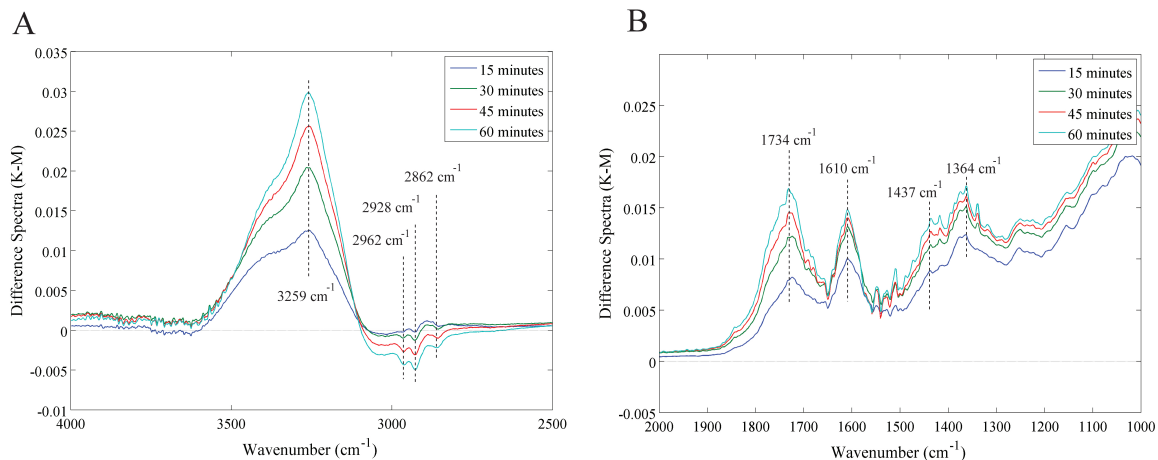
69

Figure 4.5: DRIFTS difference spectra of UV-illuminated carbon-modified TiO_2 at 15-minute intervals during the first 1 hour of photocatalytic oxidation at 200 °C. The background used to acquire these samples was the dry carbon-modified TiO_2 sample immediately prior to UV illumination.

environment. Therefore, it can be interpreted from this data that the irradiation of carbon-coated TiO_2 at lower temperatures results in the production of CO_2 (with a formic acid byproduct or intermediate) due to oxidation of amorphous carbonaceous species with photo-generated reactive hydroxyl groups.

At 200 °C, the DRIFTS results indicate a distinctly different mechanism. Rather than observing the consumption of formate and water species with increasing reaction time, adsorbed water ($3259cm^{-1}$ feature) and carboxylate species ($1734cm^{-1}$ feature, corresponding to the C=O vibration) are observed. Additional potential carboxylate features are observed at $1610cm^{-1}$ and $1437cm^{-1}$, corresponding to the asymmetric and symmetric OCO vibrations [94, 97–99]. The only spectroscopic evidence of photocatalytic hydrocarbon or carbon oxidation is the removal of CH stretching frequencies at 2962, 2928, $2862cm^{-1}$ and the increased adsorbed water peaks. In contrast to DRIFTS experiments conducted at 40 °C, the loss of terminal hydroxyl groups and the production of gas-phase CO_2 was not observed during experiments conducted at 200 °C.

The absence of hydroxyl and formate consumption during 200 °C DRIFTS experi-

70

ments suggest that photo-generated hydroxyl species are not mechanistically involved during the photocatalytic oxidation of carbonaceous species under these conditions. In fact, Hägglund, et al. described a mechanism in which, during elevated temperature photocatalytic oxidation of propane in dry air, the TiO_2 surface is dehydroxylated upon UV illumination. Therefore, propane decomposition intermediates, such as carboxylates, adsorb strongly on the dehydroxylated surface, which leads to photocatalyst discoloration [89]. In addition to DRIFTS evidence of a similar deactivation mechanism, the carbon-modified TiO_2 sample shows some signs of dehydroxylation after 48 hours of photocatalytic oxidation at 200 °C, mainly due to the slight discoloration observed in Figure 4.1.

Although the hydroxyl intermediate is not participating in the photocatalytic oxidation reaction at 200 °C, it is possible that photocatalytic oxidation might be occurring via two alternate reaction intermediates: O_2-superanions generated on exposed Ti(III) centers, or through the generation of O_2-superanion species on graphitic carbon [100]. Due to Raman spectroscopic evidence of a loss of graphitic carbon during photocatalytic oxidation at elevated temperatures and from the high surface coverage of carbonaceous species, it is proposed that the generation of O_2-superanion species over graphitic carbon is primarily responsible for photocatalytic oxidation.

The importance of water vapor during the photocatalytic oxidation of carbon and hydrocarbons cannot be understated. In the absence of water vapor, photocatalytic reaction rates are very low, primarily due to polar/non-polar adsorbate interactions of water and hydrocarbons. At elevated temperatures, the relative surface coverage of polar and non-polar compounds are more favorable to photocatalytic oxidation, however, in the absence of water vapor, dehydroxylation of the TiO_2 surface may result in the accumulation of carboxylate species, and subsequent photocatalyst deactivation. In contrast, high water vapor concentrations will limit adsorption of hydrocarbons and therefore limit photocatalytic oxidation rates. The determination of a 'maximum' wa-

ter concentration during photocatalytic oxidation reactions is difficult. As mentioned, the polarity of reactants and the photocatalyst surface dramatically affect adsorption energies, thereby influencing photocatalytic rates. In order to establish maximum oxidation rates, a balance between temperature, light intensity, water vapor and hydrocarbon partial pressures must be established, such that the photocatalyst surface is not deficient in hydroxyl groups and that it has sufficient coverage of hydrocarbons.

4.5 Conclusions

The photocatalytic oxidation of carbonaceous deposits was investigated at two temperatures (40 and 200 °C) in a novel photocatalytic reactor. Carbonaceous materials were deposited on sol-gel derived TiO_2 by the pyrolysis of hydroxyethylcellulose; Raman spectroscopy confirmed the presence of amorphous and graphitic carbon species, while DRIFTS confirmed the presence of general carboxylate species, in addition to some formate species, evidenced by additional CH stretching. Low temperature photocatalytic oxidation experiments result in a depletion of surface-bound carbon species, as witnessed by the change in Raman-visible carbon VR and G vibrations and TiO_2 E_g vibrations. Similarly, elevated temperature photocatalytic oxidation results in decreased carbon-titania ratio as the reaction progresses. The slope of the Raman-characterized carbon-titania ratio roughly expresses the observed rate of oxidation, which indicates faster oxidation rates at elevated temperatures. Mechanistically, partial deactivation of the photocatalyst occurs at elevated temperatures resulting from the dehydroxylation of the TiO_2 surface and subsequent accumulation of carboxylate species. This accumulation prevents photo-generated hydroxyl radical formation and carbon oxidation by hydroxyl radicals. However, oxidation is suspected to continue over partially deactivated photocatalysts via an O_2-superanion intermediate. Although carbon photocatalytic oxidation rates are low over TiO_2, enhancements may be found by increasing catalyst temperatures to thermally overcome

72

kinetic activation barriers. However, reactant humidity and surface hydroxyl concentration play a crucial role in overall photocatalyst activity, behavior, and potential for widespread application.

CHAPTER V

High-Temperature Photocatalytic Oxidation of Ethylene over TiO$_2$ [2]

5.1 Abstract

Photocatalytic oxidation of ethylene was conducted in a novel two-dimensional packed bed reactor at higher temperatures (60 °C < T < 520 °C) than previously reported. Degussa P25 TiO$_2$ was used as a photocatalyst; samples of this TiO$_2$ were heat treated to different temperatures to obtain different phase compositions, surface areas, and surface hydroxyl concentrations. Maximum photocatalytic ethylene oxidation rates were observed between 100 °C to 200 °C. Further, oxidation rates greater than 75% of the maximum oxidation rate were observed over a large temperature range: 60 °C < T < 300 °C. At higher temperatures (T > 300 °C), decreasing oxidation rates were attributed to the non-radiative, multi-phonon recombination of photo-generated charge carriers. Regression analysis of a nonlinear, multi-phonon recombination model and a simplified chemical rate law were used to determine apparent reaction rate law parameters for the photocatalytic oxidation of ethylene and recombination parameters for the TiO$_2$ photocatalyst. Insights for the development and operation of novel high-temperature photocatalysts are also discussed.

5.2   Introduction

The necessity to find a more efficient TiO_2 photocatalyst has driven the investigation of the photocatalytic behavior of mixed-phase TiO_2 photocatalyst, Degussa P25. This commercially available TiO_2 exhibits excellent photocatalytic activity compared to other TiO_2 photocatalysts. Possible reasons for enhanced photocatalytic activity include: surface area, crystalline phase composition, surface hydroxyl concentration, and interfacial charge transfer dynamics [101? –106]. Many of these characteristics are confounded with each other and the photocatalysts heat treatment temperature. Prevailing hypotheses for enhanced photocatalytic activity of P25 surround the electronic states (location of the conduction and valence bands) of anatase and rutile TiO_2 phases in contact with each other in the photocatalyst, and charge transfer mechanisms that effectively separate charge carriers [107–110].

Charge carriers are produced when a photocatalyst absorbs a photon with sufficient energy: a valence electron is promoted to the conduction band, leaving a hole in the valence band. Recombination of these charge carriers is a major contributor to the inefficiency of photocatalysts [5, 7, 111–114]. Finding a way to increase the charge carrier lifetimes would be important, as it would lead to the increased availability of reactive electrons and holes on the surface of the catalyst, which in turn would increase photocatalytic efficiencies. Increasing the carrier lifetime can be achieved very simply with the addition of metals, usually through photo-reduction of metal salts over the photocatalyst, or via simple metal impregnation methods [5, 112, 114, 115]. Other methods for increasing photocatalyst efficiencies rely on the optimization of electron and hole mobility, which increases the time the charge carrier spends on the photocatalyst surface, rather than in the bulk photocatalyst [5, 107, 111, 112, 116, 117].

In TiO_2 - based photocatalytic oxidation mechanisms, such as photocatalytic remediation of volatile organic compounds (VOCs), the species primarily responsible

for oxidation chemistry is the photo-generated hole [3, 84, 111, 115, 118]. Photo-generated electrons migrate to regions in the catalyst with Fermi energy lower than that of the semiconductor, such as a metal (Au or Pt), while the holes migrate to photocatalyst defects and surface vacancies [117]. At the surface of the photocatalyst, the photo-generated hole is free to oxidize an adsorbed species, such as molecular oxygen, a surface hydroxyl, or adsorbed water molecule to produce O_2-superanion, or hydroxyl radical; both species are responsible for the decomposition of adsorbed hydrocarbons into mineral acids and CO_2 [3, 84, 105, 111–113, 118].

As photocatalytic oxidation reactions are generally thought to be non-activated processes [111, 119, 120], they should be temperature independent. However, oxidation temperature influences photocatalytic oxidation rates for several VOCs due to changes in adsorption energy of polar and non-polar reactants (e.g. water and ethylene) [111, 113, 119, 121, 122]. Analysis of experimental ethylene photocatalytic oxidation rates, for example, reveals an apparent activation energy of approximately 12.13 kJ/mol [119, 123, 124]. Multiple studies have observed maximum rates of photocatalytic ethylene oxidation between 50-110 °C [119, 123–126]. However, these investigations do not comment on the effects of further increasing the oxidation temperature beyond 110 °C. In the limit of high temperature, charge carrier recombination dynamics should dramatically limit the number of charge carriers present on the photocatalyst surface. Knowledge from the solid-state physics literature can be used in the analysis of such high-temperature recombination processes. Non-radiative, multi-phonon recombination of photo-generated charge carriers become significant at photocatalyst temperatures equivalent to and larger than the Debye temperature of the photocatalyst ($\theta_D = 327$ °C and 247 °C, for rutile and anatase TiO_2, respectively [127]), [128, 129]. Up to now, the published research was limited to photocatalyst testing at temperatures too low to fully observe the effects of such recombination dynamics (e.g., T < 110 °C).

The purpose of this study is to investigate the high-temperature photocatalytic oxidation rates of ethylene over TiO_2 photocatalysts. Insights on the non-radiative, multi-phonon recombination rates of charge carriers in TiO_2 photocatalysts can also be inferred from the analysis of high-temperature ethylene oxidation rate data. Ethylene was chosen as a probe VOC, because it is a parent molecule of other, more hazardous compounds, such as trichloroethylene. A unique photocatalytic reactor was constructed for this purpose, consisting of a very thin, flat catalyst bed (bed dimensions: 0.5mm x 30mm x 30mm). The large area of the catalyst bed is illuminated on one side and heated from the opposing side. This configuration allows independent control of catalyst bed temperature and illumination of the catalyst bed according to the experimental conditions. Additional reactor details, such as CAD drawings and flow modeling results can be found in the supplementary information.

5.3   Experimental

The TiO_2 photocatalyst (Degussa P25) was calcined at either 200 °C, 400 °C, 600 °C, 700 °C or 800 °C for 4 hours in air to produce catalysts with a varied phase composition. These catalysts were then deposited on Davasil Silica Gel (35-60 mesh, Sigma-Aldrich #236802) that had been calcined at 800 °C in air for 4 hours. The deposition procedure involved physical mixing of the calcined TiO_2 and SiO_2 (to achieve a 5wt%TiO_2/SiO_2 loaded catalyst), followed by the submersion of the catalyst in deionized water and 20 min of ultrasonication. The mixed catalysts were then dried overnight in an oven at 120 °C. Characterization was conducted on the calcined, unsupported TiO_2 catalysts. Single-point BET surface areas were measured in a Quantachrome ChemBET-3000. Phase analysis of the anatase and rutile structures was calculated from XRD data, according to [104]. Differential Scanning Calorimetry (DSC) was conducted on a TA Q600 TGA/DSC to determine amorphous phase content [130–132]. These experiments were conducted in an air

environment at a heating rate of 40 °C/min. Diffuse Reflectance UV/Vis (DRUV/Vis) Spectroscopy of each TiO_2 sample was acquired on a ThermoScientific Evolution 300 UV-Visible Spectrophotometer. The determination of surface hydroxyl concentration was conducted in a thermogravimetric analysis instrument (TA Q500) using ammonia desorption. A $1\%NH_3$ in N_2 gas stream was introduced to the dried catalyst for 60 minutes, followed by a 60 minute purge with UHP N_2, followed by a temperature programmed desorption ramp from 100 °C to 800 °C. The mass of desorbed ammonia was used as a measure of the surface hydroxyl concentration, using a 1:1 ratio of hydroxyl groups to adsorbed ammonia.

A model of the photocatalytic reactor used for oxidation experiments was designed in SolidWorks and tested for uniform temperature distributions and gas flow distributions across the catalyst bed using COMSOL Multiphysics simulations (Figures 3.6 & 3.7). The simulation demonstrated sufficient uniformity in both temperature and gas velocity profiles across the catalyst bed. The reactor was machined out of stainless steel and heated by 4 1/4 cartridge heaters, which were controlled by LabVIEW software. The illuminated side of the catalyst bed was sealed from the laboratory environment by a 1.0cm-thick section of GE 124 quartz (Technical Glass Products, 90% transmission at 365nm). Quartz wool packing on the influent and effluent ends of the catalyst bed prevented channeling of the gas stream and immobilized the catalyst throughout the duration of the experiment. Figure 3.8 shows the flow reactor loaded with photocatalyst. UV illumination was achieved via a UV spot lamp (Blak-Ray B 100AP) located 10cm from the catalyst bed. Intensity measurements taken under the quartz window showed that the catalyst bed received $25mW/cm^2$ of 365nm illumination.

In a typical experiment, 125mg of catalyst was loaded into the photocatalytic reactor, which was then sealed by the compression of a graphite gasket between the reactor body and the quartz window; a leak test was conducted to ensure a complete

seal. The photocatalytic reactor was then wrapped in insulating glass wool, and the UV lamp positioned above the catalyst bed. Inlet gas consisted of 50sccm dry air, 3sccm ethylene (99.9%), and 50sccm argon diluent. Gas flow rates and diluent concentrations were set to achieve minimal thermal ethylene conversion ($X_{Ethylene} < 5\%$) at the highest temperatures studied. The reactant stream was then passed through a DI water saturator at room temperature before entering the photocatalytic reactor. External mass transfer effects were negligible, as observed by independent rate measurements with respect to the square root of total flow rate over a range of space velocities a factor of 2 about the experimental flow rate.

A temperature program was built into the LabVIEW control software to ensure repeatability of experiments. The catalyst was first heated to 200 °C for 2 hours to establish an acceptable equilibrium of gas-phase components over the catalyst bed. The catalyst was then allowed to cool to 60 °C before starting the experiment. At each temperature step, oxidation rate data were acquired for 45 min with the UV lamp off, followed by 45 min with the UV lamp on. These rate data represent oxidation rates of the thermal process and the thermal plus photocatalytic process, respectively. The temperature steps during photocatalytic oxidation experiments were: 60 °C, 100 °C, 170 °C, 250 °C, 325 °C, 360 °C, 400 °C, 440 °C, 480 °C, and 520 °C, as measured in the center of the catalyst bed. Experiments with smaller temperature increments were introduced at higher temperatures to better discriminate photocatalytic oxidation rates from thermal oxidation rates, as the thermal oxidation rates become equivalent to or greater than the measured photocatalytic rates.

Oxidation rates were measured by quantifying effluent CO_2 concentrations via a Bruker Optics FTIR equipped with a gas flow cell. Carbon dioxide concentrations were measured by the integration of the experimental CO_2 peak area (2400cm^{-1} 2300cm^{-1}) and calibrated to the CO_2 peak area of a 500ppm CO_2 standard. The CO_2 peak area calibration curve was found to be linear with respect to CO_2 concentration

across the experimentally observed range of CO_2 concentrations.

A diffuse reflectance infrared spectrometer (DRIFTS) accessory was used in the Bruker Optics FTIR to assess the presence of surface hydroxyl species before and after high temperature photocatalytic oxidation reactions. In this experiment, a 1wt% TiO_2/KBr sample (600 °C TiO_2 calcination temperature) was loaded into the DRIFTS cell, and heated to 200 °C for 30 minutes in dry nitrogen to remove physically adsorbed water. The sample was then cooled to 20 °C in dry nitrogen and a DRIFTS spectrum of the dry TiO_2 catalyst was recorded at $2cm^{-1}$ resolution with 512 scans. The DRIFTS-mounted sample was then exposed to the reactant gas stream (C_2H_4, O_2, H_2O, and Ar), UV illumination, and 600 °C catalyst bed temperature for 1 hour. After 1 hour duration, the reactant gas was replaced by dry nitrogen, and the bed temperature was lowered to 200 °C for 30 minutes to remove water from the catalyst bed. A final spectrum was taken once the sample had cooled to 20 °C under dry nitrogen.

5.4 Results

Single-point BET surface area measurements of each calcined TiO_2 photocatalyst (Table 5.1) gave values similar to those reported in literature. Surface hydroxyl concentrations and XRD phase analysis results are also presented in Table 5.1, while the Raman and XRD spectra are shown in Figure 5.1.

Amorphous, anatase, and rutile phase compositions were calculated from XRD and DSC data. Amorphous to anatase phase transitions were observed between 388-400 °C for samples calcined to 200 and 400 °C, while no transition was observed for samples calcined at higher temperatures; these results are consistent with previously reported phase transition behavior [130–132]. The rutile and amorphous TiO_2 phase compositions were strongly dependent on calcination temperature. DRUV/Vis spectroscopy confirmed that the band gap energies for each sample followed the expected

80

Table 5.1: Photocatalyst characterization results

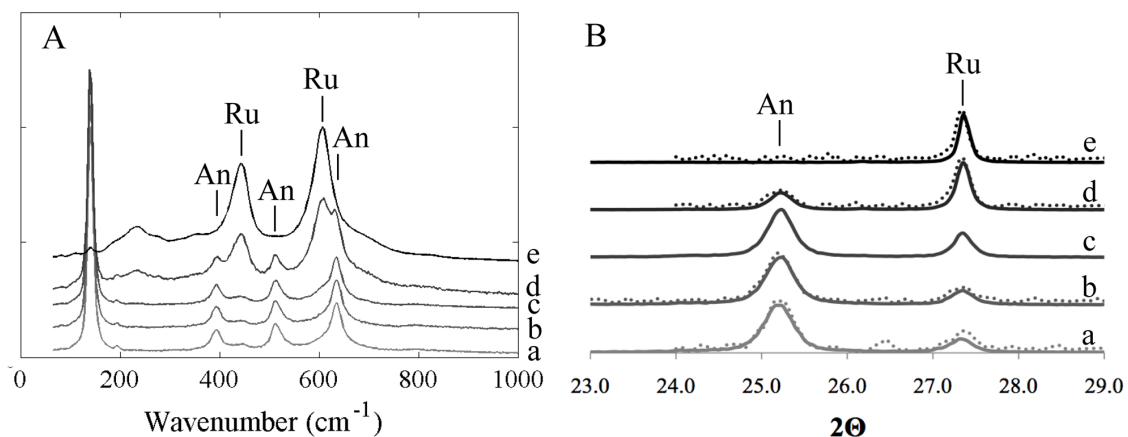| Calcination Temperature	Surface Area $(m^2\ g^{-1})$	[OH] $(\mu mol\ g^{-1})$	Phase Content (wt% amorphous / anatase / rutile)	Band Gap Energy (eV)
200°C	52.2 ($\pm$0.6)	9.0 ($\pm$2.8)	10.6/65.4/24.0 ($\pm$6.2/4.5/1.7)	2.96
400°C	52.2 ($\pm$0.5)	6.6 ($\pm$3.0)	2.5/70.2/27.4 ($\pm$2.5/1.4/0.6)	2.96
600°C	45.4 ($\pm$0.6)	5.3 ($\pm$1.9)	0/60.6/39.4 ($\pm$0.5/0.6/0.7)	2.94
700°C	27.2 ($\pm$0.5)	5.0 ($\pm$2.2)	0/22.3/77.7 ($\pm$NA/0.6/0.7)	2.91
800°C	11.2 ($\pm$0.2)	4.0 ($\pm$2.9)	0/1.1/98.9 ($\pm$NA/0.6/0.7)	2.88

Figure 5.1: Raman (A) and XRD (B) spectra of photocatalysts calcined at 200 °C (a), 400 °C (b), 600 °C (c), 700 °C (d), 800 °C (e). Peak positions of anatase and rutile are marked with An, and Ru, respectively. Post-reaction diffraction data is presented as dotted lines in the XRD data.
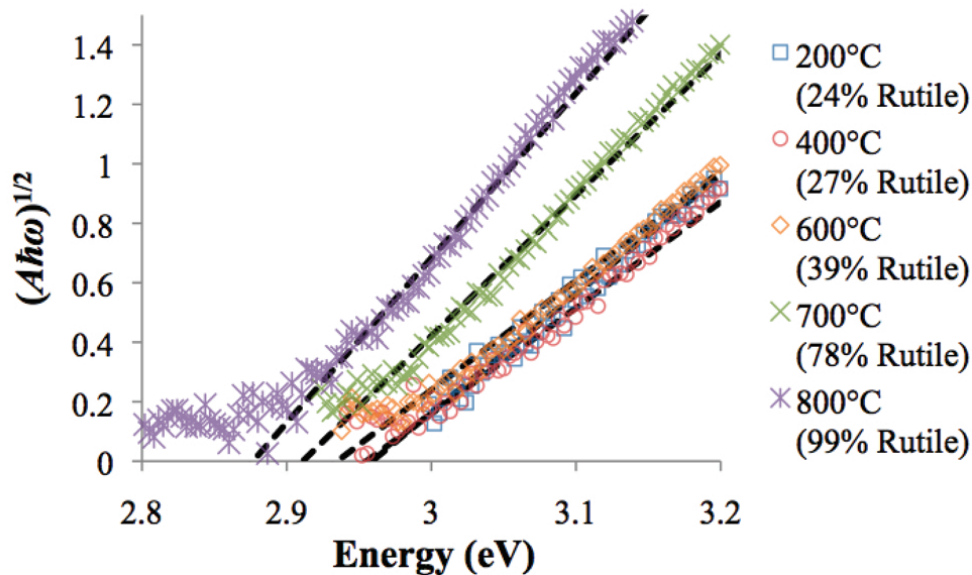
Figure 5.2: Determination of the indirect band transitions of calcined photocatalysts using UV/Vis Reflectance Spectroscopy results.

trends: DRUV/Vis results are shown in Figure 5.2, while band gap energies are shown in Table **??**. Experimental data for the photocatalytic oxidation of ethylene are presented in Figure 5.3.

The inset of Figure 5.3 illustrates the calculation of the photocatalytic oxidation rate; the oxidation rate in the absence of UV illumination was subtracted from the oxidation rate during UV illumination at each experimental oxidation temperature. It should be noted that two of the five catalysts, namely the 200 °C and 400 °C calcined catalysts, were tested for photocatalytic oxidation at temperatures which exceeding their respective calcination temperatures. In an effort to extract useful information from oxidation results of these catalysts, phase analysis was conducted on the post-reaction XRD patterns for every catalyst. The pre- and post-reaction phase composition results are used as the bounds for error bars on the averaged phase composition for all data discussed in the following sections.

All catalysts exhibited an exponential increase in thermally oxidized ethylene with increased reaction temperature. The addition of UV photons contributed to ethylene
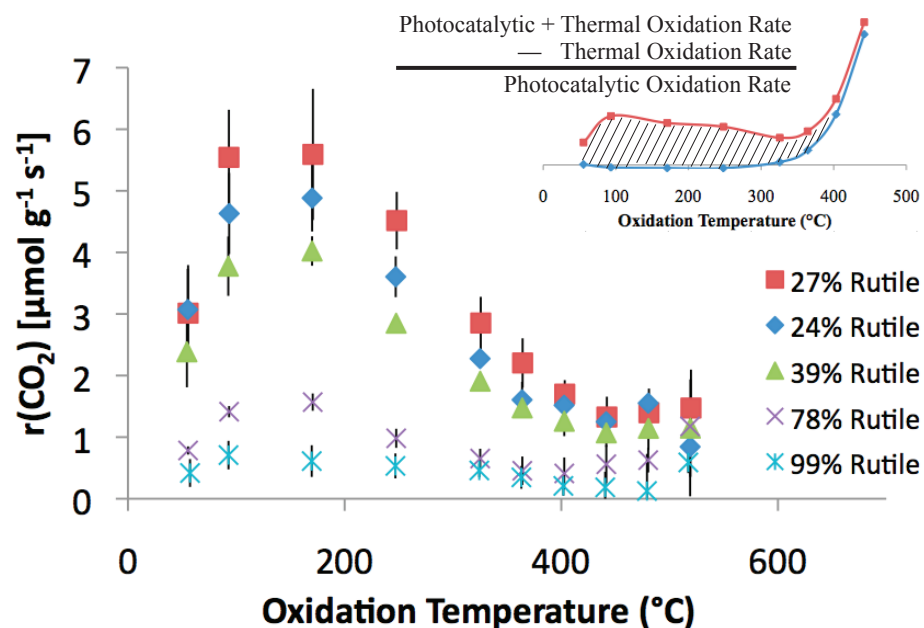
Figure 5.3: Experimental photocatalytic oxidation data for all five TiO_2 catalysts. Inset shows the calculation of photocatalytic oxidation rates from raw experimental data.

conversion at low and moderate temperatures (T<325 °C), however, as the temperature increased, the presence of UV photons had a diminished effect. As shown in Figure 5.3, the photocatalytic oxidation rates reached a maximum between 100-200 °C and decreased to near-zero values at 500 °C.

The presence of surface hydroxyl groups after reaction was confirmed by the independent DRIFTS experiment. Figure 5.4 shows the OH-stretching region of the acquired spectra; the native TiO_2 hydroxyl groups remained after 1 hour of photocatalytic oxidation at 600 °C.

5.5   Discussion

Maximum photocatalytic ethylene oxidation rates were observed between 100 °C and 200 °C for all catalysts tested. To exactly pinpoint the temperature for maximum oxidation rates would require additional experiments with smaller temperature
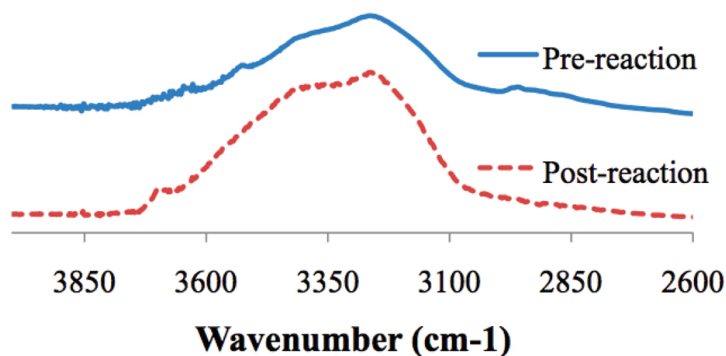
Figure 5.4: DRIFTS results before and after 1 hour photocatalytic ethylene oxidation over 400 °C calcined TiO_2.

increments: however, the observations made with the current set of temperatures are sufficient to confirm that the maximum oxidation rate occurs above the previously reported temperature range of 60-110 °C.The observed trend of increased oxidation rates at temperatures less than 200°C were due to differences in ethylene and water adsorption energies on the polar Ti-OH surface [124]; increased oxidation temperature shifts the adsorbate concentrations closer to stoichiometric ratios, thereby increasing ethylene oxidation rates.

The loss of photocatalytic activity at high temperatures can be attributed to the loss of either of two photocatalytic intermediate species: surface hydroxyl groups or photo-generated charge carriers. Photo-generated charge carriers and surface-bound hydroxyl groups are directly involved in the oxidation mechanism [3, 111, 123]. The results of the DRIFTS experiment show that surface hydroxyl groups persist on the TiO_2 catalyst after 60 minutes of photocatalytic oxidation at high temperature and ethylene conversion (Figure **??**). Therefore, the decreasing photocatalytic activity above 200 °C must be due to the loss of photo-generated charge carriers.

The loss of photo-generated charge carriers can take place through multiple routes; the most relevant recombination pathways include radiative and non-radiative recom-

bination. Photoluminescence emission spectroscopy, for example, measures the energy of emitted photons from the radiative recombination of photo-generated charge carriers. In non-radiative recombination, inelastic collisions between charge carriers and phonons result in lost charge carrier energy. Non-radiative interactions typically involve multiple phonon participation in large band gap materials and occur with increasing probability as temperatures increase, due to the increase in the population of high-energy phonons and in the interphonon interaction rates (most notably the three-phonon interactions). Non-radiative, multi-phonon recombination pathways have been well-characterized for lasing materials, such as doped Ti^{3+}:Al_2O_3, and Yb^{3+}:Y_2O_3 [128] as well as in other luminescence-based chemistries [133].

The temperature dependence of both recombination pathways are of particular interest to the current investigation: the rate of radiative recombination (γ_{Rad}) is independent of temperature, while the rate of non-radiative recombination ($\gamma_{Non-Rad}$) is dependent on temperature [134] and is shown in Eq. (5.1) [129].

$$\gamma_{Non-Rad} = \gamma_{Rad(T=0K)} \left(1 - e^{\frac{-\hbar\omega_p}{k_B T}}\right)^{-N_p} \tag{5.1}$$

Here, the average phonon energy is represented by $\hbar\omega_p$, while N_p represents the number of phonons participating in recombination. The prefactor, $\gamma_{Rad(T=0K)}$, is the radiative recombination rate at zero Kelvin, due to the lack of phonons and non-radiative recombination at zero Kelvin. Equation (5.1) assumes the non-radiative recombination is controlled by the equilibrium occupancy of a phonon with this energy, and not by its rate of conversion (up or down) toward equilibrium [135].

Equation (5.1) can be used to derive a modified oxidation rate equation, based on fundamental knowledge of photocatalytic rate equations. For instance, a hallmark feature of a photocatalytic rate law is the dependence of rate on the illumination intensity (I) and the quantum efficiency (ϕ). Quantum efficiency is the ratio of

radiative decay rate to the sum of radiative and non-radiative decay rates, and is usually calculated as ratio of the rate of moles of product formed ($\gamma_{Products}$) to the rate of moles of sufficiently energetic incident photons, which is proportional to the rate of charge carrier generation (γ_{e^-/h^+} Formation), as in Eq. (5.2).

$$\phi \propto \frac{\gamma_{Products}}{\gamma_{e^-/h^+\,Formation}} \tag{5.2}$$

Under steady state illumination, the accumulation of charge carriers should be negligible (Eq. (5.3)). Therefore, the rate of recombination of charge carriers (γ_{Recomb}) should equal the rate of generation of charge carriers, i.e.,

$$\frac{d(e^-/h^+)}{dt} = 0 = \gamma_{e^-/h^+\,Formation} - \gamma_{Recomb} \tag{5.3}$$

Three charge carrier recombination pathways are relevant at the temperatures investigated here: radiative recombination (γ_{Rad}), non-radiative recombination ($\gamma_{Non-Rad}$), and charge transfer to intermediate species with the final result of product formation (Eq. (5.4)), i.e.,

$$\gamma_{Rcomb} = \gamma_{Rad} + \gamma_{Non-Rad} + \gamma_{Products} \tag{5.4}$$

Given Eqs. (5.2)-(5.4), the quantum efficiency can be rewritten as in Eq. (5.5).

$$\phi \propto \frac{\gamma_{Products}}{\gamma_{e^-/h^+\,Formation}} = \frac{\gamma_{Products}}{\gamma_{Rad} + \gamma_{Non-Rad} + \gamma_{Products}} \tag{5.5}$$

Due to the high occupancy of the high energy phonons emitted in the multi-phonon emission at elevated temperatures ($\gamma_{Non-Rad} >> \gamma_{Rad} + \gamma_{Chem}$) [104], the quantum efficiency can be simplified and combined with Eq. (5.1) to reflect temperature effects on quantum efficiency (Eqs. (5.6) & (5.7)) and we have

$$\phi \propto \frac{\gamma_{Products}}{\gamma_{Non-Rad}} = \frac{\gamma_{Products}}{\gamma_{Rad(T=0K)}} \left(1 - e^{\frac{-\hbar\omega_p}{k_B T}}\right)^{N_p} \tag{5.6}$$

$$\phi = k_\phi \left(1 - e^{\frac{-\hbar\omega_p}{k_B T}} \right)^{N_p} \tag{5.7}$$

where k_ϕ is the temperature-independent quantum efficiency term. Therefore, introduction of the temperature-dependent quantum efficiency term (Eq. (5.7)) into a generic photocatalytic ethylene oxidation rate equation produces Eq. (5.8),

$$r_{CO_2} = 2k_{App} P_{C_2H_4}^\alpha P_{O_2}^\beta P_{H_2O}^\delta I \left(k_\phi \left(1 - e^{\frac{-\hbar\omega_p}{k_B T}} \right)^{N_p} \right) \tag{5.8}$$

In Eq. (5.8), k_{App} is the apparent rate constant and the partial pressures of reactants and products are represented. This rate equation simplifies to a four-term model if the partial pressures of reactants and products are held constant for each experiment at different temperatures. The total ethylene conversion was limited below 5% at 520 °C oxidation temperature, therefore, the simplified photocatalytic oxidation model is shown in Eq. (5.9) using an apparent activation energy E_{App} and a combined pre-exponential term, i.e.,

$$-r_{CO_2} = k_{App,\phi} e^{\frac{-E_{App}}{RT}} \left(1 - e^{\frac{-\hbar\omega_p}{k_B T}} \right)^{N_p} \tag{5.9}$$

We note that the phonon participation is only represented through the occupancy of energy p and the kinetics of interphonon interactions that include the density of states (or the Debye temperature under assumption of no dispersion) are not considered. A complete treatment should apply the Fermi golden rule as for example in [135]. We also note that instead of the bulk phonons on the TiO_2 substrate, we should consider surface phonons that couple with the frustrated motion of the adsorbates. So, we expect Eq. (5.9) to be a rough first approximation of the process.

Nonlinear regression was performed in MATLAB using the nlinfit tool. A poor fit was obtained for the regression of the 4-parameter model to the experimental data. Therefore, it was necessary to reduce the number of model parameters. The appar-
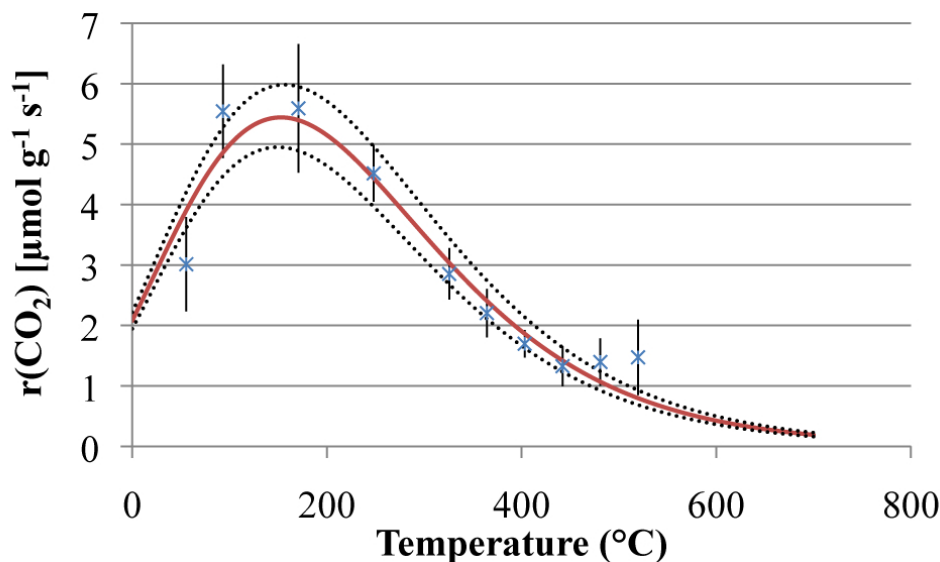
Figure 5.5: Results from nonlinear regression of Eq. (5.9) on experimental photocatalytic oxidation data over TiO_2 calcined to 400 °C. Solid lines represent the regressed model, while dotted lines represent the regressed model with standard error estimates of the fitted parameters.

ent activation energy for ethylene photocatalytic oxidation is generally agreed to be approximately 3.0 kcal/mol (12.13 kJ/mol) [118, 119, 121]. Therefore, this parameter was fixed. The 3-parameter nonlinear regression produced acceptable results; the regressed parameters and their standard error estimates are shown in Table 5.2 along with the r-squared values for each fit. Results from the regression are plotted with experimental data in Figure 5.5.

Arrhenius interpretation of the photo-thermal and thermal ethylene oxidation data taken from the TiO_2 photocatalyst calcined to 400 °C (Figure 5.6) reveals that the photo-thermal oxidation of ethylene can follow two distinct reaction mechanisms, depending on photocatalyst temperature. At low temperatures, the oxidation is a photo-active process with a small activation energy (approximately 13 kJ mol^{-1}), while at higher temperatures, the photo-thermal oxidation of ethylene appears to appears to have a similar mechanism as thermal oxidation and has a much higher activation energy (approximately 100 kJ mol^{-1}).
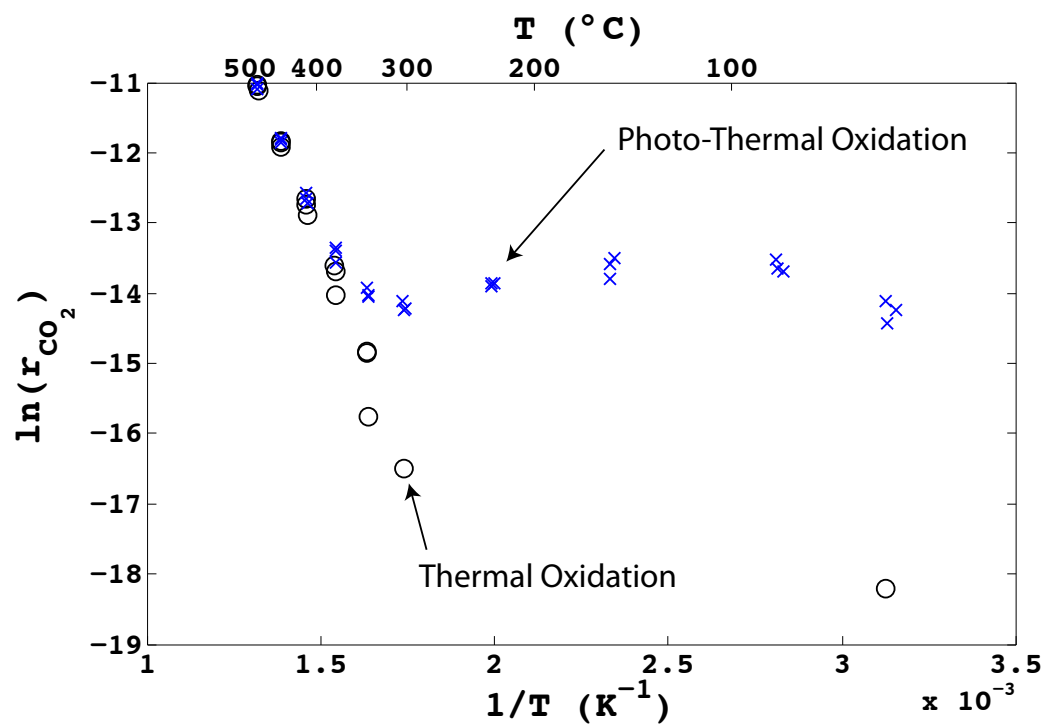
Figure 5.6: Arrhenius plot of photocatalytic ethylene oxidation over TiO_2 calcined to 400 °C.

Table 5.2: Nonlinear regression results

Calcination Temperature	$k_{App,\phi}$ (μmol g^{-1} s^{-1})	E_{App} (kJ mol^{-1})	$\hbar\omega_p$ (meV)	N_p	r^2
200°C	273.6 (260.2,286.9)	12.13	94.9 (93.8, 96.0)	17	0.94
400°C	563.8 (534.6, 593.2)	12.13	100.2 (99.0, 101.5)	18	0.93
600°C	207.9 (198.1, 217.8)	12.13	98.9 (97.9, 100.0)	18	0.94
700°C	82.3 (75.3, 89.3)	12.13	96.3 (94.3, 98.3)	18	0.88
800°C	35.1 (33.1, 37.2)	12.13	98.0 (96.6, 99.3)	17	0.91

The modeled rate equation (Eq. (5.9)) effectively separates rate effects due to chemical kinetic limitations and charge carrier limitations. Analysis of the regressed model parameters reveal information about the temperature-dependent and -independent terms for a range of TiO$_2$ phase compositions. For instance, the pre-exponential factor, k_{App}, ϕ, represents the lumped temperature-independent terms of the kinetic apparent pre-exponential factor, reactant and product partial pressures, temperature-independent quantum efficiency, and illumination intensity. Pressure terms and illumination intensity terms were assumed to be independent of catalyst phase. Therefore, the regressed pre-exponential factor for each catalyst reflects changes in the kinetic apparent pre-exponential factor and/or the temperature independent quantum efficiency term. Figure 5.7A shows the regressed pre-exponential factor as a function of the measured catalyst rutile phase.

The product of the kinetic apparent pre-exponential term with the temperature-independent quantum efficiency term results in an observed linear trend with respect to catalyst phase. In addition, the use of the measured surface hydroxyl species concentration as a normalization parameter produced regressed parameters which were also phase dependent (Figure 5.7B). These observations agree with previous observations of phase-dependent photocatalytic activity of TiO$_2$ [107–110].

Information regarding charge carrier recombination dynamics can also be gleaned from analysis of the regressed phonon energy ($\hbar\omega_P$) and phonon number (N_p) parameters. The density of phonon density of states for both anatase and rutile TiO$_2$ were
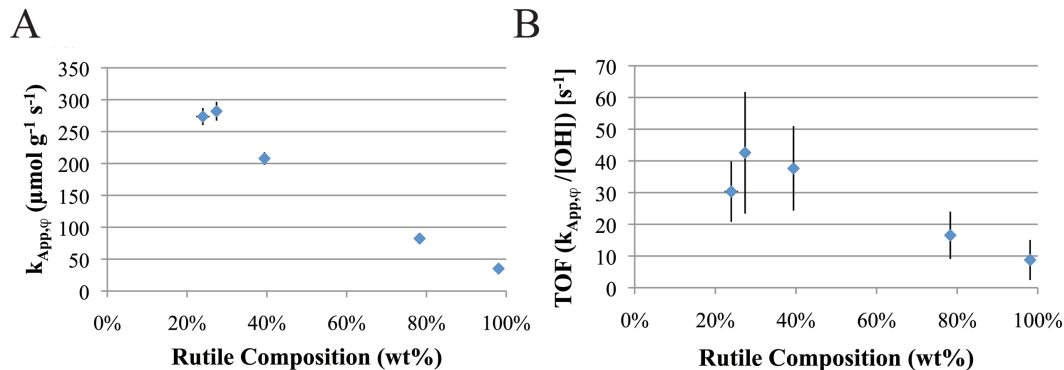
Figure 5.7: Fitted pre-exponential factors (A) for each catalyst, plotted as a function of the rutile phase content in each catalyst. The pre-exponential factors have been reported as a function of the catalyst mass. Turn over frequency (B), calculated from the normalization of the regressed pre-exponential factor (A) with the measured surface hydroxyl concentration (mol g^{-1}) determined from NH_3-desorption experiments.

calculated and reported in [136]; depending on the calculation method used, the maximum phonon energies are 810-875 cm^{-1} (100-109 meV) and 780-825 cm^{-1} (97-102 meV), respectively [136]. The regressed phonon energy values, shown in Table 5.2, are approximately 10-20 meV below the predicted maximum phonon energies for TiO_2. The standard error on the regression parameters reveals insignificant correlation of phonon energy to phase composition, which was expected, given the close relation of phonon density of states between rutile and anatase phases of TiO_2. Additionally, the regressed parameter for the number of phonons participating in charge carrier decay, N_p, range between 17 and 18, at or below i.e., the accepted maximum of 18 phonons [137].

A common correlation between the phonon energy and number of participating phonons in non-radiative, multi-phonon recombination processes is the Energy Gap Law (EGL). The EGL states that the product of the phonon energy with the number of phonons is equal to the dissipated charge carrier energy [138]. The total energy dissipated due to non-radiative decay will be referred to as the EGL dissipation energy; the EGL dissipation energy for each of the photocatalysts tested varies between 1.60
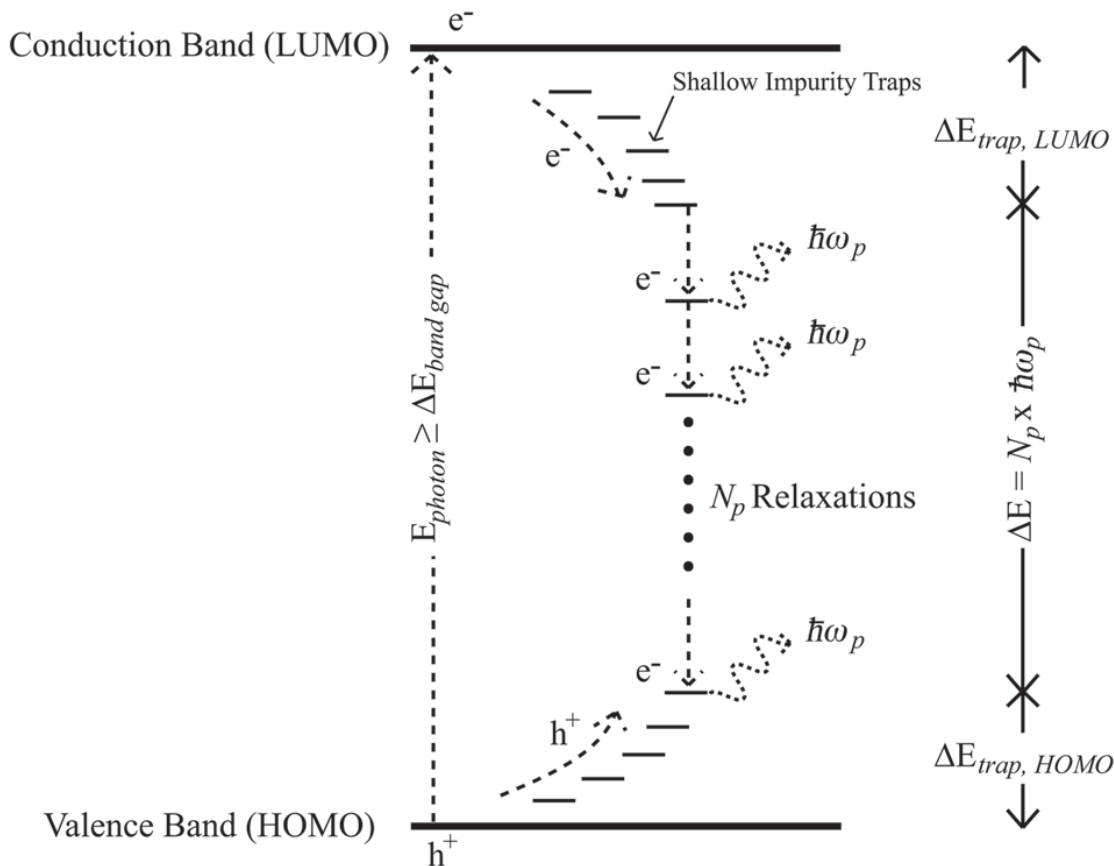
Figure 5.8: Diagram of photon absorption and charge formation and the charge carrier relaxation (recombination) processes, showing the traditional band gap energy, trap and defect energy levels, and the multi-phonon relaxation process which takes place with increased probability at higher temperatures.

eV and 1.80 eV. The difference in energy between the TiO_2 band gap, measured by DRUV/Vis, and the EGL dissipation energy can be attributed to energy loss of the charge carrier due to defects and trap states present in the photocatalyst. Electronic trap states are common, especially in mixed-phase solids, such as P25 [102]. While many of these trap states occupy energy levels hundreds of meV below the conduction band, some have been reported as low as 1.5 eV below the conduction band of anatase TiO_2 [139]. A schematic of the combined decay processes is presented in Figure 5.8.

This schematic illustrates photo-generated electron transfer from the conduction
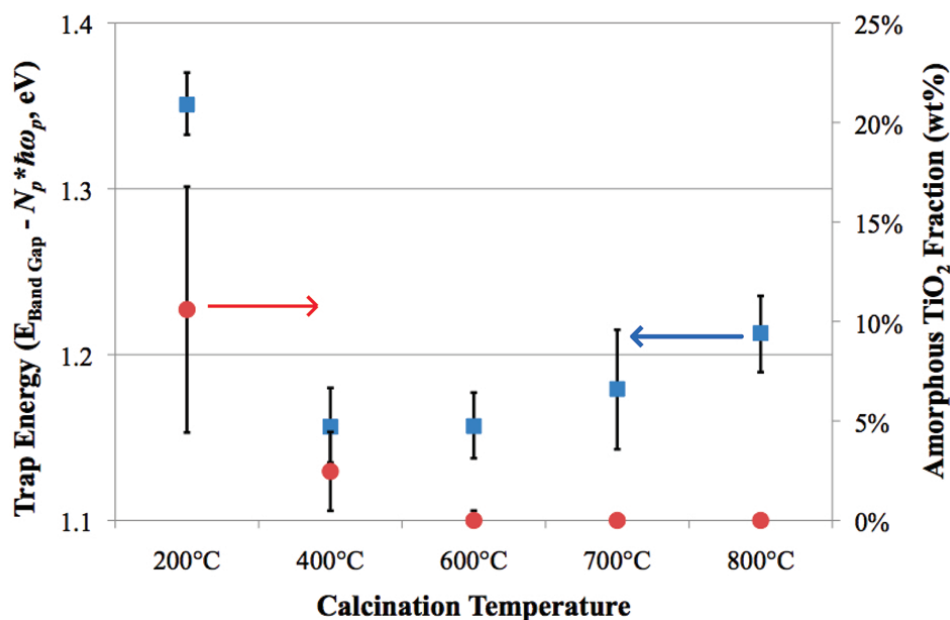
Figure 5.9: The energy lost to trap states, calculated from the subtraction of the energy lost via multi-phonon recombination (via the Energy Gap Law) from the measured band gap energy and the measured amorphous TiO_2 phase content, measured via DSC. Each promoted electron contains an energy equivalent to the band gap energy, however the Energy Gap Law can only account for a fraction of the non-radiative recombination energy. The difference in recombination energy can be attributed to the energy of recombination lost to charge carrier decay to trap and impurity states.

band to lower energy trap states. At elevated temperatures, the electron can undergo non-radiative, multi-phonon decay into hole trap states, which lie slightly above the valence band. Although the non-radiative decay occurs instantaneously and emits N_p phonons, the process is shown piecewise in Figure 5.8 for simplicity. The trap energy ($E_{Trap} = E_{bandgap} \quad E_{EGLDissipation}$) for the five catalyst calcination temperatures is shown in Figure 5.9.

The catalyst calcined at 200 °C exhibits the largest band gap energy and the lowest EGL dissipation energy, and therefore the largest trap energy. The 200 °C calcination sample also exhibited the maximum content of amorphous TiO_2, as determined by DSC measurements. This suggested that the 200 °C calcined catalyst contained

significantly deeper-lying trap states than the other catalysts. Further, calcination to 400 °C removes these trap sites or impurities without dramatically changing the observed band gap energy (Table 5.1). Therefore, the presence of heavy trap states in the 200 °C calcined sample is most likely due to the presence of amorphous TiO_2, which may be removed by heat treatment above the amorphous-to-anatase phase transition, at approximately 400 °C.

Extension of this analysis can be used to guide the development of photocatalysts designed to operate more efficiently at elevated temperatures. For example, current VOC oxidation photocatalysts have been shown to operate with a maximum photocatalytic rate between 60-200 °C [2, 119, 123–126]. Equation (5.9) predicts that Degussa P25 operating between 60-200 °C has an effective quantum efficiency approximately 25-60% of its maximum quantum efficiency, due to non-radiative, multiphonon recombination dynamics. Given a wide range of tunable variables, such as band gap energies, trap, vacancy or impurity states, and phonon dispersion characteristics, high-temperature photocatalysts could be designed to be less affected by non-radiative recombination limitations, thus improving elevated temperature photocatalytic operating efficiencies.

5.6 Conclusions

The aim of this work was to understand fundamental limitations of high-temperature photocatalytic reactions using the photocatalytic oxidation of ethylene as a probe reaction. A novel high-temperature photocatalytic reactor was designed and constructed in order to achieve high catalyst bed temperatures while maximizing the illuminated photocatalyst bed area. The photocatalyst tested was a heat-treated Degussa P25 TiO_2, which contained different anatase and rutile phase compositions than the commercially available powder. Photocatalytic oxidation experiments showed that the photocatalyst achieved significant oxidation rates at catalyst bed tempera-

tures of up to 350°C. The maximum photocatalytic oxidation rate was observed between 100-200°C; higher photocatalyst temperatures resulted in a decreased oxidation rate. The decline in photocatalytic activity can be attributed to the non-radiative, multi-phonon recombination of charge carriers which was modeled by an exponential function of temperature and two bulk TiO_2 properties: phonon energy and phonon participation number. Further, the fitted model parameters from the non-linear regression analysis are physically reasonable and can be used to simultaneously extract information regarding temperature independent photocatalytic activity and electronic trap states of the photocatalyst. Using this information, photocatalysts designed with specific phonon energy, phonon number, band gap energy, and trap states could be engineered with decreased high-temperature charge-carrier recombination rates. This could lead to catalysts with increased photocatalytic VOC oxidation efficiencies at elevated temperatures.

CHAPTER VI

Extension of High Temperature Photo-activity Model to Alternate Photochemical Systems

6.1   Introduction

In the previous chapter, a succinct correlation of photocatalytic activity with photocatalyst temperature was developed. This relation used specific semiconductor crystal information to predict the activity of TiO_2 for photocatalytic oxidation of ethylene as a function of temperature. However, a more general model should be capable of accurately predicting activity trends across multiple chemistries and multiple photocatalysts. In an effort to explore the accuracy of the generalization of this model, it was applied to three alternate photocatalytic oxidation systems. As a first system, photocatalytic oxidation of ethylene in dry air was investigated, and the effects of varying water vapor concentrations were explored as a first test of the applicability of this model for other chemistries. The presence of water vapor in the reactant stream is expected to have significant effects on photocatalytic oxidation activity over TiO_2, as seen already during the oxidation of carbonaceous deposits over TiO_2, described earlier in this thesis.

As a second system, the effects of an alternate photocatalyst (ZnO, band gap = 3.3eV) on the photocatalytic oxidation of ethylene were explored. And finally as a

third system, the effects of an alternate hydrocarbon (propylene) on its photocatalytic oxidation over TiO_2 were explored.

In each experiment, 125mg of catalyst was loaded into the photocatalytic reactor, which was then sealed by the compression of a graphite gasket between the reactor body and the quartz window; a leak test was conducted to ensure a complete seal. The photocatalytic reactor was then wrapped in insulating glass wool, and the UV lamp positioned above the catalyst bed. Inlet gas consisted of 50sccm dry air, 3sccm of either ethylene or propylene (99.9%), and 50sccm argon diluent. During the photocatalytic oxidation of ethylene over ZnO or in the case of propylene oxidation over TiO_2, a room temperature water saturator humidified the reactant gas stream. Gas flow rates and diluent concentrations were set to achieve minimal thermal ethylene conversion ($X_{Ethylene} < 5\%$) at the highest temperatures studied. External mass transfer effects were negligible, as observed by independent rate measurements with respect to the square root of total flow rate over a range of space velocities a factor of 2 about the experimental flow rate. Error bars shown in each figure are the result of three independent measurements of oxidation rate over different catalyst beds and represent the standard error associated with every section of the experimental protocol, save for the synthesis of the photocatalyst.

A temperature program was built into the LabVIEW control software to ensure repeatability of experiments. The catalyst was first heated to 200°C for 2 hours to establish an acceptable equilibrium of gas-phase components over the catalyst bed. The catalyst was then allowed to cool to 60°C before starting the experiment, and then the photocatalytic activity was measured at a range of temperatures; the temperature steps during photocatalytic oxidation experiments were: 60°C, 100°C, 170°C, 250°C, 325°C, 360°C, 400°C, 440°C, 480°C, and 520°C, as measured in the center of the catalyst bed. At each temperature step, oxidation rate data were acquired for 45 min with the UV lamp off, followed by 45 min with the UV lamp on. These rate data

97

represent oxidation rates of the thermal process and the thermal plus photocatalytic process, respectively. Experiments with smaller temperature increments were introduced at higher temperatures to better discriminate photocatalytic oxidation rates from thermal oxidation rates, as the thermal oxidation rates become equivalent to or greater than the measured photocatalytic rates.

Oxidation rates were measured by quantifying effluent CO_2 concentrations via a Bruker Optics FTIR equipped with a gas flow cell. CO_2 concentrations were measured by the integration of the experimental CO_2 peak area ($2400cm^{-1}$ $2300cm^{-1}$) and calibrated to the CO_2 peak area of a 500ppm CO_2 standard. The CO_2 peak area calibration curve was found to be linear with respect to CO_2 concentration across the experimentally observed range of CO_2 concentrations.

6.2   Photocatalytic Ethylene Oxidation over TiO_2: Effects of Humidity

Photocatalytic oxidation of hydrocarbons is typically very dependent on humidity [105, 119, 124]. This effect manifests itself due to the non-polar and polar nature of hydrocarbons and water, respectively and their respective bonding with the polar TiO_2 surface. The relatively stronger hydrogen bonding of water and TiO_2 results in a photocatalyst surface that is predominantly covered by water or hydroxyl groups and thus limited in its ability to react with hydrocarbons, due to their low surface coverage. On the other hand, surfaces that have low surface coverage by water can become poisoned by incomplete oxidation byproducts, such as carboxylate and formate structures. Therefore, many researchers in the photocatalytic oxidation community have explored this effect of water surface coverage with the aim of finding a maximum rate of photocatalytic oxidation [105, 119, 123–125, 140].
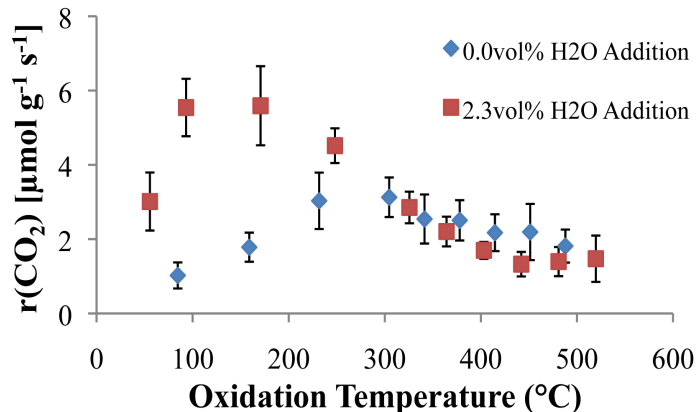
Figure 6.1: Effect of water addition on the photocatalytic oxidation rate of ethylene over TiO_2 calcined to 400°C.

6.2.1 Results

The experimental data are shown in Figure 6.1 (TiO_2 calcined to 400 °C, for the cases of no water addition and 2.3vol% water addition, for comparison with data from Chapter 5) and Figure 6.2 (TiO_2 calcined at 200, 400, 600, and 800 °C, or 24, 27, 39 and 99wt% rutile, respectively).

6.2.2 Discussion & Conclusions

Nonlinear regression fitting of the temperature-dependent photocatalytic ethylene oxidation rate equation (Equation 6.1) resulted in good agreement between model and experimental data (shown in Figure 6.3, $r^2 = 0.95$). In light of the findings of Chapter 5, notably, that the photocatalytic activity as a function of temperature can be accurately approximated using known phonon dispersion parameters, $\hbar\omega_p$, and N_p., these values were fixed in this regression. Therefore, 2 parameters were regressed in the present situation, $k_{App,\phi}$ and $E_{a,apparent}$. The regressed parameters are shown in Table 6.1, which also shows regression results from a similar experiment with water
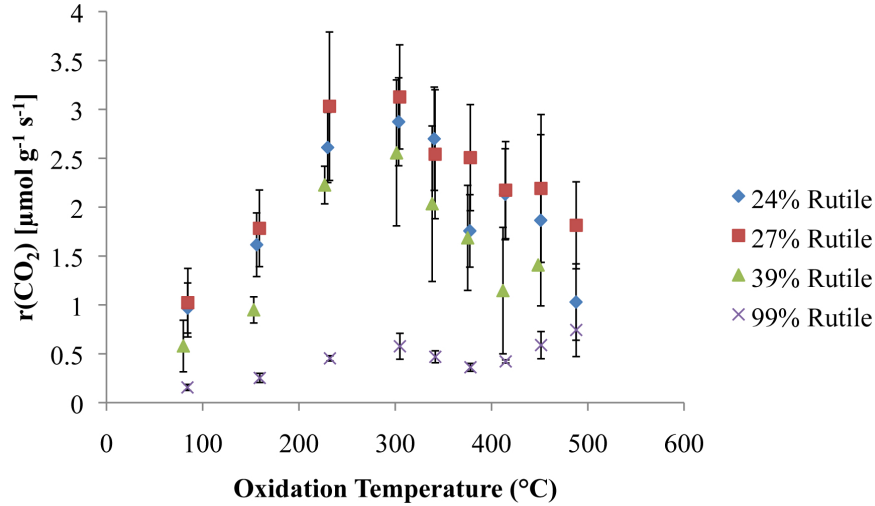
Figure 6.2: Photocatalytic oxidation rate of ethylene over TiO_2 catalysts calcined to 200, 400, 600, and 800°C in a dry air stream.

addition by a room temperature water saturator.

$$-r_{CO_2} = k_{App,\phi} e^{\frac{-E_{App}}{RT}} \left(1 - e^{\frac{-\hbar\omega_p}{k_B T}} \right)^{N_p} \tag{6.1}$$

The experimental and modeling results for all four calcined photocatalysts are shown in Figure 6.5, below; all r^2 values were above 0.88.

The nonlinear regression exercises reveal that the key parameter to the modeling of alternate reaction schemes (in this example, alternate water concentrations during the photocatalytic oxidation of ethylene) is the apparent activation energy, $E_{a,apparent}$. In fact, algebraic manipulation of the photocatalytic ethylene oxidation rate equation proposed by Yamazaki, et al [123], reveals that the apparent activation energy is actually a summation of the apparent activation energy, as well as enthalpies of adsorption for ethylene, water, and oxygen. Therefore, it is expected that the apparent activation energy would appear to change when the concentration of water and hydrocarbons is altered. T. Obee, et al, stated very clearly in a report published in 1997 that the photocatalytic oxidation of ethylene should be a non-activated process,

Table 6.1: High temperature photocatalytic recombination model parameters for ethylene oxidation over TiO_2 with and without water addition to the reactant stream. Parameters from the oxidation of ethylene in 2.3vol% H_2O over TiO_2 calcined to 400°C (27% Rutile) is shown for comparison.

Water Content	$k_{App,\phi}$ (μmol g^{-1} s^{-1})	E_{App} (kJ mol^{-1})	$\hbar\omega_p$ (meV, Constant)	N_p (Constant)
0.0% H_2O (24% Rutile)	2462	23.0	95.0	18
0.0% H_2O (27% Rutile)	2538	23.0	95.0	18
0.0% H_2O (39% Rutile)	1872	23.0	95.0	18
0.0% H_2O (99% Rutile)	316.8	23.0	95.0	18
2.3% H_2O (27% Rutile)	563.9	12.13	95.0	18
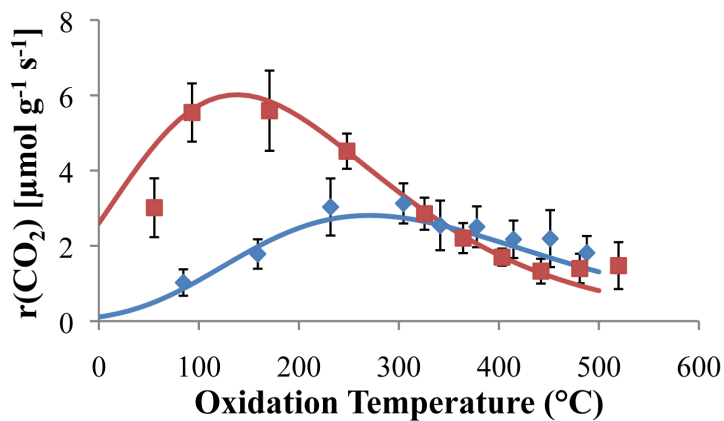
Figure 6.3: Results of nonlinear regression model fitting on data observed in Figure 6.1.
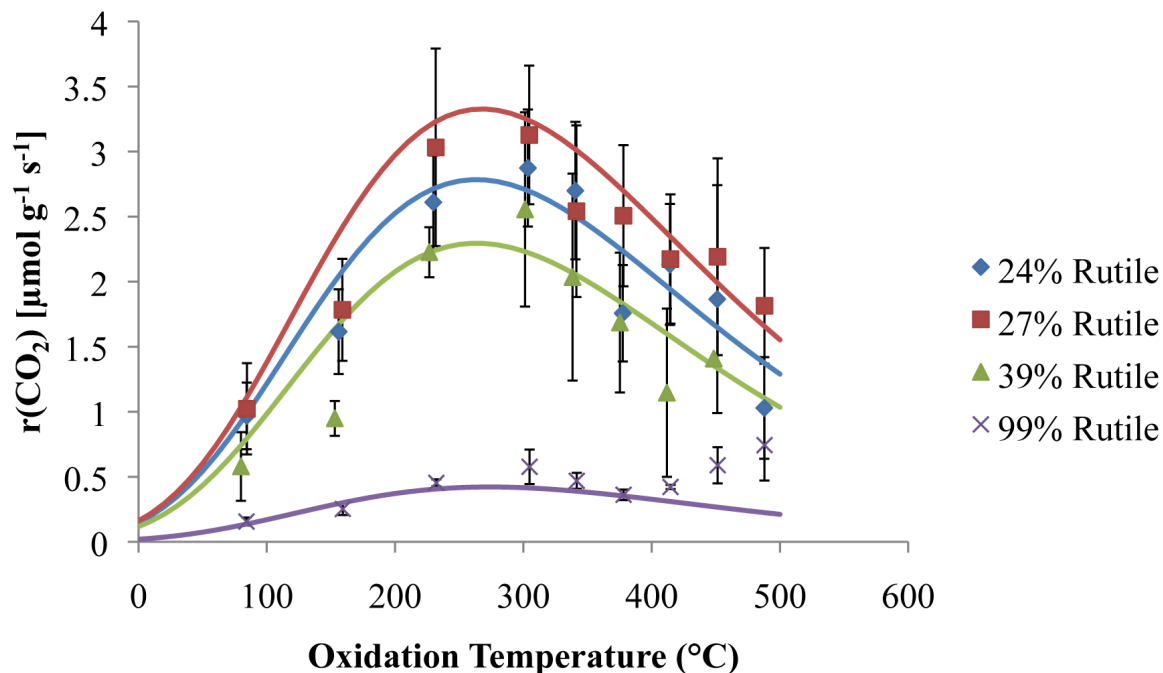
Figure 6.4: Results of nonlinear regression model fitting on data observed in Figure 6.2.

and the observed differences in activation energies are due to adsorption enthalpy effects [119] − a finding which supports the conclusions of this work.

6.3 Photocatalytic Ethylene Oxidation over ZnO

Another test of the temperature-dependent photocatalytic ethylene oxidation rate equation and its ability to explain experimental results in light of the effects of multi-phonon recombination is the photocatalytic ethylene oxidation experiment over an alternate photocatalyst, ZnO.

6.3.1 Results

The photocatalytic oxidation rate of ethylene over ZnO is shown in Figure 6.5, along with the oxidation rate over TiO_2, for comparison. Due to the low relative
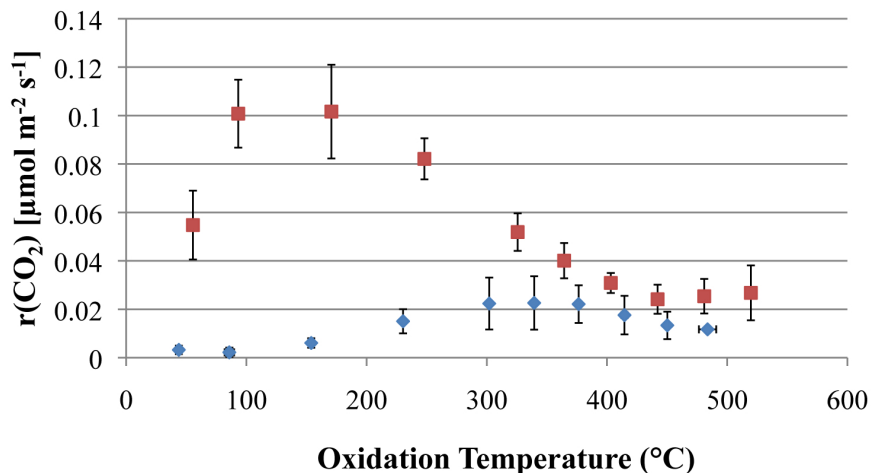
Figure 6.5: Comparison of photocatalytic oxidation rate over TiO_2 (red) and ZnO (blue).

Table 6.2: High temperature photocatalytic recombination model parameters for ethylene oxidation over TiO_2 and ZnO.

Support	$k_{App,\phi}$ (μmol g^{-1} s^{-1})	E_{App} (kJ mol^{-1})	$\hbar\omega_p$ (meV, Constant)	N_p (Constant)
TiO_2	563.9	12.13	95.0	18
ZnO	1596	27.9	73.0	12

photocatalytic activity of ZnO, as compared to TiO_2, the oxidation rate is normalized by the photocatalyst surface area, rather than by photocatalyst mass, as previously done.

6.3.2 Discussion & Conclusions

Nonlinear regression parameters fit to data in Figure 6.5 are shown in Table 6.2, while the regressed model is shown in Figure 6.6. The regression resulted in a reasonable fit to experimental data, with an r^2 value of 0.80.

The alteration of the apparent activation energy in Equation 6.1 to include enthalpy of adsorption effects is a simple and effective strategy to predict photocatalytic behaviors of any semiconductor as a function of temperature. As shown here, the replacement of semiconductor-specific phonon dispersion parameters to Equation 6.1
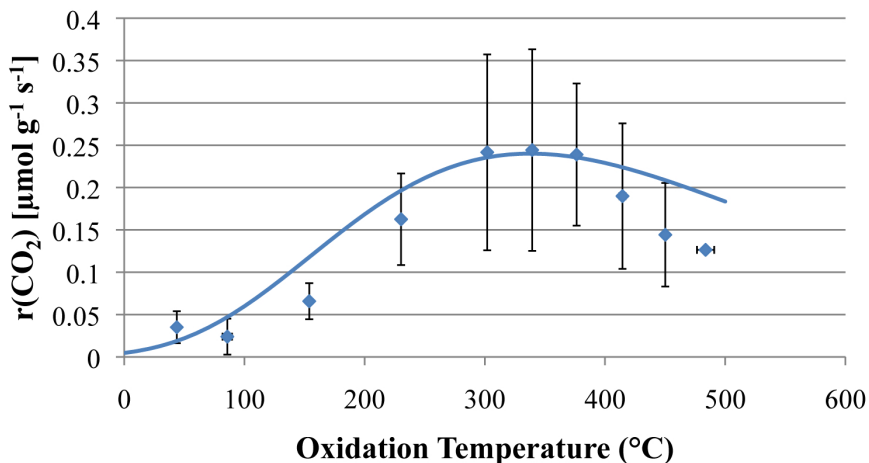
Figure 6.6: Results of nonlinear regression model on data from Figure 6.5.

results in an accurate prediction of photocatalytic ethylene oxidation rates over multiple photocatalysts as a function of temperature. The photocatalyst-independent nature of this model is extremely powerful in explaining, and possibly predicting, photocatalytic activity as a function of temperature.

6.4 Photocatalytic Carbon Monoxide Oxidation over Au/TiO$_2$

6.4.1 Introduction

So far, this thesis has focused primarily on studying the recombination dynamics of semiconductor photocatalysts at elevated temperatures. This work has led to a fundamental understanding of the limitations of pure semiconductors as they pertain to photocatalysis, or even high temperature photocatalysis. The obvious extension of this work is to metal-loaded semiconductor photocatalytic systems.

For instance, there exist many industrially relevant catalytic reactions that rely on a metal supported on a photocatalyst. In fact, TiO$_2$ can be used as a support for many water-gas-shift, hydrogenolysis, and partial oxidation catalysts.

Metal particles added to a semiconductor photocatalyst generally act as an elec-

tron trap, which can lead to increased photocatalytic activity due to the increased separation distance between photogenerated holes and electrons [102, 103, 106, 109, 141, 142]. However, in order for the metallic particles to act as an electron trap, photogenerated electrons must first migrate from the bulk crystal phase to the metal-semiconductor interface.

Metal-loaded semiconductor photocatalysis has been shown to improve photocatalytic rates (due to charge separation) [143]; however, it has not yet been explored to what extent thermal catalytic reaction rates on supported metal catalysts can be photocatalytically enhanced. Recently, the photocatalytic activity of semiconducting TiO_2 has been investigated in the temperature range from room temperature to more than 500°C [2].

To measure the photocatalytic enhancement of a thermally-driven catalytic reaction over a supported catalyst, CO oxidation over Au/TiO_2 was investigated. Catalytic oxidation of CO is a unique reaction, due its chemical simplicity, elusive reaction intermediates, and potential application in fuel cell gas clean-up and other preferential oxidation applications [144–146].

6.4.2 Materials and Methods

The catalyst used for photocatalytic oxidation of carbon monoxide was Au supported on TiO_2. Chloroauric acid was dissolved in a 10:1 solution of DI water and ethanol, Degussa P25 TiO_2 was added to the solution and allowed to stir for 30 minutes at room temperature. The photoreduction of Au onto TiO_2 was conducted by illuminating the solution with UV light. The solution was then centrifuged, resuspended in clean DI water and centrifuged again. The Au/TiO_2 was then dried at 120°C overnight, ground, dispersed onto silica gel (35-60 mesh, post 800°C, 4hr calcination in air to remove internal porosity), and calcined at 500°C for 1hr.

In each experiment, 125mg of catalyst was loaded into the photocatalytic reactor,

which was then sealed by the compression of a graphite gasket between the reactor body and the quartz window; a leak test was conducted to ensure a complete seal. The photocatalytic reactor was then wrapped in insulating glass wool, and the UV lamp positioned above the catalyst bed. Inlet gas consisted of 100sccm a gas mixture containing $1\%CO/10\%O_2$ and a nitrogen balance. The photocatalytic reactor was ramped in temperature from $25°C$ to $400°C$ at a rate of $2.5°C/min$ without UV illumination. The reactor was then cooled back to room temperature and the same catalyst was tested with an identical procedure with UV illuminating the photocatalyst. Again, the photocatalyst was cooled and the reaction was repeated a third time without UV illumination to check for any catalyst deactivation in the course of the 2 previous experiments. Once completed, another identical temperature ramp experiment was conducted on bare TiO_2 without UV illumination to determine the contribution of bare TiO_2 photocatalytic oxidation rates on the previously obtained CO-oxidation rates.

Oxidation rates were measured by quantifying effluent CO_2 concentrations via a Bruker Optics FTIR equipped with a gas flow cell. CO_2 concentrations were measured by the integration of the experimental CO_2 peak area ($2400cm^{-1}$ $2300cm^{-1}$) and calibrated to the CO_2 peak area of a 500ppm CO_2 standard. The CO_2 peak area calibration curve was found to be linear with respect to CO_2 concentration across the experimentally observed range of CO_2 concentrations.

6.4.3   Results & Discussion

TEM and STEM analysis reveals that the Au metal particle size varied between 20nm and 50nm; these images are shown in Figure 6.8. Therefore the photoreduction metal deposition technique employed herein did not result in a narrow distribution of gold particle size. However, temperature programmed reaction results over the Au/TiO$_2$ catalysts indicate that UV illumination significantly improves CO conver-
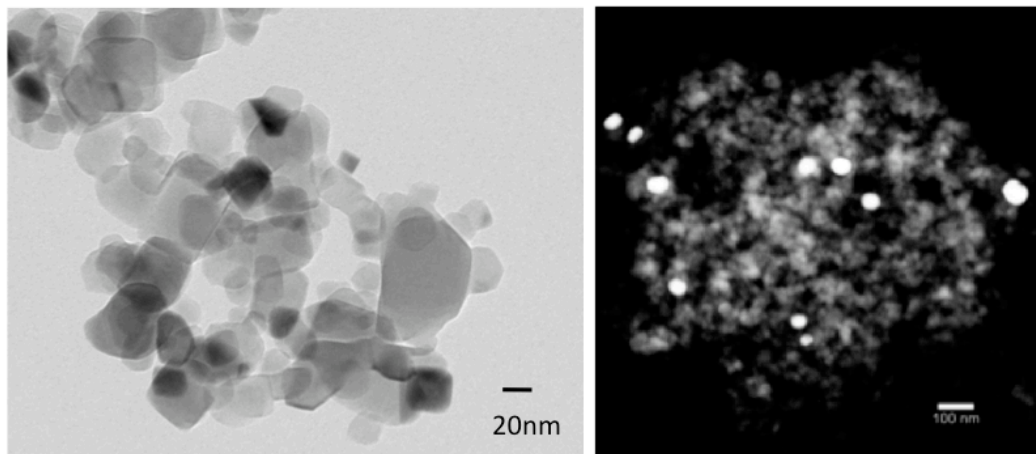
Figure 6.7: TEM (left) and STEM (right) images of synthesized Au/TiO$_2$ catalysts. Scale bars are 20nm and 100nm, for TEM and STEM images, respectively.

sion in the range of 100-250°C (Figure 6.8).

Bare TiO$_2$ was also tested under CO-TPR to assess the photocatalytic oxidation activity of the blank support as a function of temperature (Figure 6.8). Previous oxidation experiments with ethylene have shown that the effective quantum efficiency of a semiconductor such as TiO$_2$ decreases with temperature per Equation 6.1 [105]. As no photocatalytic oxidation activity exists at room temperature (Figure 6.8), the observed oxidation activity of bare TiO$_2$ at elevated temperatures is thermally-driven. Addition of Au results in a significant enhancement of oxidation activity in the presence of UV illumination. This is not merely an additive effect of multiple oxidation reaction mechanisms; rather, it suggests a synergistic effect.

Arrhenius interpretation of the data reveals very similar apparent activation energies (60.4 and 59.1 kJ mol^{-1} for the thermal and photo-thermal cases, respectively); however, under UV illumination, the pre-exponential term is approximately 2.4 times greater than the pre-exponential term in the thermal case (Figure 6.9).
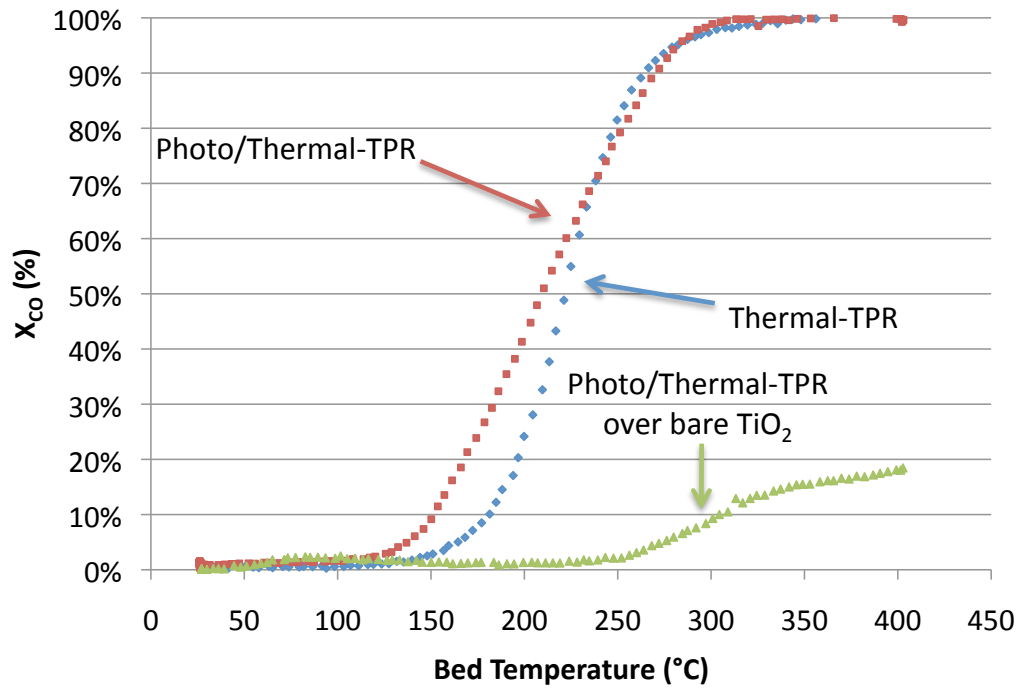
Figure 6.8: Temperature programmed carbon monoxide oxidation over Au/TiO_2 with (Red) and without (blue) UV illumination and over bare TiO_2 with UV illumination (Green).
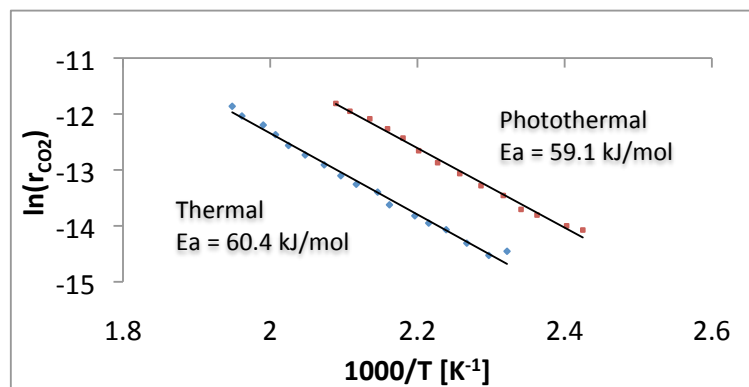
Figure 6.9: Arrhenius graph of carbon monoxide oxidation rates with and without UV illumination. Data plotted here represents carbon monoxide conversion between 2 and 15%.

6.4.4   Conclusions

The utilization of a photocatalytic mechanism to promote thermally-driven reactions have never been observed on metal-loaded semiconductors, although, this effect has been observed over plasmon-resonant metal particles [87], as well as over bare semiconductors [2]. Temperature programmed reaction and Arrhenius data interpretation reveal the high activity of UV illuminated Au/TiO_2. The potential application of photocatalysis to thermally-driven catalysis is far-reaching. However, without significant improvement in photocatalyst phonon dispersion parameters (to reduce recombination rates at elevated temperature), photo-thermal catalysis will be limited to an upper limit of $300-400°C$. Fortunately, many industrially relevant reactions occur below these temperatures, such as ammonia production, ethylene epoxidation, and carbon monoxide selective oxidation.

CHAPTER VII

Conclusions

In the second chapter of this thesis, carbon deposition during steam reforming of isooctane over nickel catalysts was investigated. Carbon deposition is a very relevant problem for hydrogen production. A carbon deposition mitigation strategy that would allow continued reformer operation would be of particular interest to the hydrogen production industry, as it would significantly increase reformer efficiencies. Photocatalysis offers new insight for carbon mitigation pathways. Lee and Choi [8] showed that soot, as deposited by a hexane flame on a TiO_2 substrate, could be photocatalytically removed at room temperature. Mills, et al. presented similar results from the photo−oxidation of butane-derived soot on a TiO_2 substrate[9].

In the third chapter of this thesis, the requirements of a photocatalytic reactor operating at elevated temperatures were explored and tested, both *in silico* and *in operando*. In order to observe relevant data, it was important to ensure that the photocatalytic reactions operate within a chemically kinetic reaction regime. The developed photocatalytic reactor and control scheme were then used in the remaining work to conduct photocatalytic reaction measurements for different reactions, from photocatalytic oxidation of carbon deposits to the photocatalytic oxidation of hazardous compounds.

Due to the complexities of elevated temperature photocatalysis, a simple analog

of reformer carbon mitigation was discussed in the fourth chapter: the photocatalytic oxidation of carbon. A more detailed investigation of the mechanisms of elevated temperature photocatalysis was pursued in the fifth chapter: a photocatalytic probe reaction, ethylene photocatalytic oxidation was employed to assess photocatalytic activity as a function of temperature. As a result of this investigation, it is now possible to state that the photocatalytic activity, or quantum efficiency, as defined in the photocatalysis community, can be described using a simple equation, whose parameters include fundamental photocatalyst phonon dispersion parameters. This simple relation allows the scientist or engineer to determine the effective photocatalyst efficiency as a function of temperature. Additionally, photocatalytic oxidation activity was observed to increase as a function of temperature. This increased rate is most likely a result of adsorption enthalpy effects between ethylene, oxygen, and water, as shown in Chapter 6.

In the latter section of Chapter 6, a very relevant catalytic reaction was explored as a prospective photo-thermal catalytic test reaction. Indeed, the photo−thermal reaction showed improved carbon monoxide oxidation rates over a Gold−Titania photocatalyst, as compared to the a thermal reaction over the same catalyst. This initial result suggests the feasibility of photo−thermal catalysis in a range of new areas, such as preferential CO oxidation, elevated temperature water splitting, ammonia production, or even carbon mitigation during reforming reactions.

The theme of this thesis is to lay the fundamental building blocks of high temperature photocatalysis − specifically for photo−thermal processes. Such processes are envisioned to replace energy intensive, inefficient, large−carbon−footprint chemical processes with a solar−thermal and solar−photocatalytic process. Future photo-thermal catalysis must be focused on one of two targets: 1) optimization of current, hydrocarbon-based catalysis (such as carbon mitigation, preferential CO oxidation, or use of solar furnaces to complete photo−thermal catalysis or reforming), or 2) De-

velopment of semiconductor−based photosynthetic production of high-value (energy or monetary) chemicals which were originally made entirely by hydrocarbon sources. However, although minor progress has been made toward this goal [2, 87], much more research is needed.

APPENDICES

APPENDIX A

Photocatalytic Reactor Specifications

A.1   Photocatalytic Reactor Engineering Drawings

Figure A.1: Dimensioned engineering drawing for the bottom section of the photocatalytic reactor designed and tested in Chapter 2 of this thesis, and used in Chapters 3, 4, 5, and 6 for photocatalytic experiments.
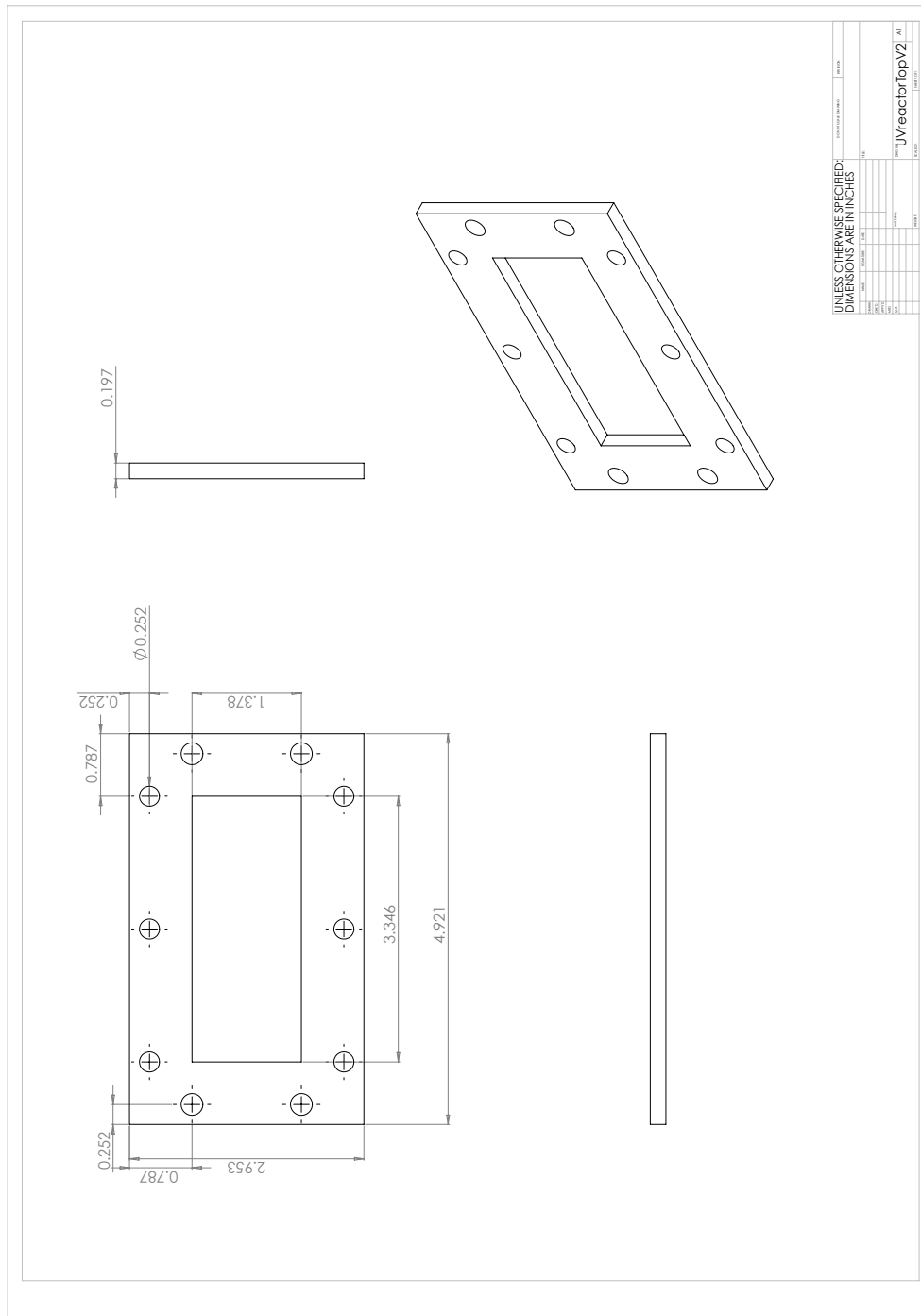
Figure A.2: Dimensioned engineering drawing for the top section of the photocatalytic reactor designed and tested in Chapter 2 of this thesis, and used in Chapters 3, 4, 5, and 6 for photocatalytic experiments.

APPENDIX B

Analytical Instrument Specifications and Operation

B.1   Infrared Quantification of CO_2

The experiments performed in Chapters 5, 6, & 7 require analytical instruments to monitor the evolution of carbon dioxide, as this was the common product. The most senstive method of quantification of CO_2 is the infrared method. According to the Beer-Lampert Law, the absorbance of light (due to the presence of an absorbing analyte) is proportional to the absorbtivity of the analyte and the path length of the flow cell. Therefore, the sensitivity of the IR analysis is directly related to the path length of the flow cell (as the molar absorbtivity of CO_2 cannot be changed).

A gas flow cell was designed and built to maximize CO_2 sensitivity in the Bruker Optics Infrared Spectrometer currently residing in the laboratory. A photograph of the flow cell is shown in B.1. The flow cell is made of three parts: A quartz tube with inlet and outlet ports, and two sodium chloride plates used as IR-transparent windows.
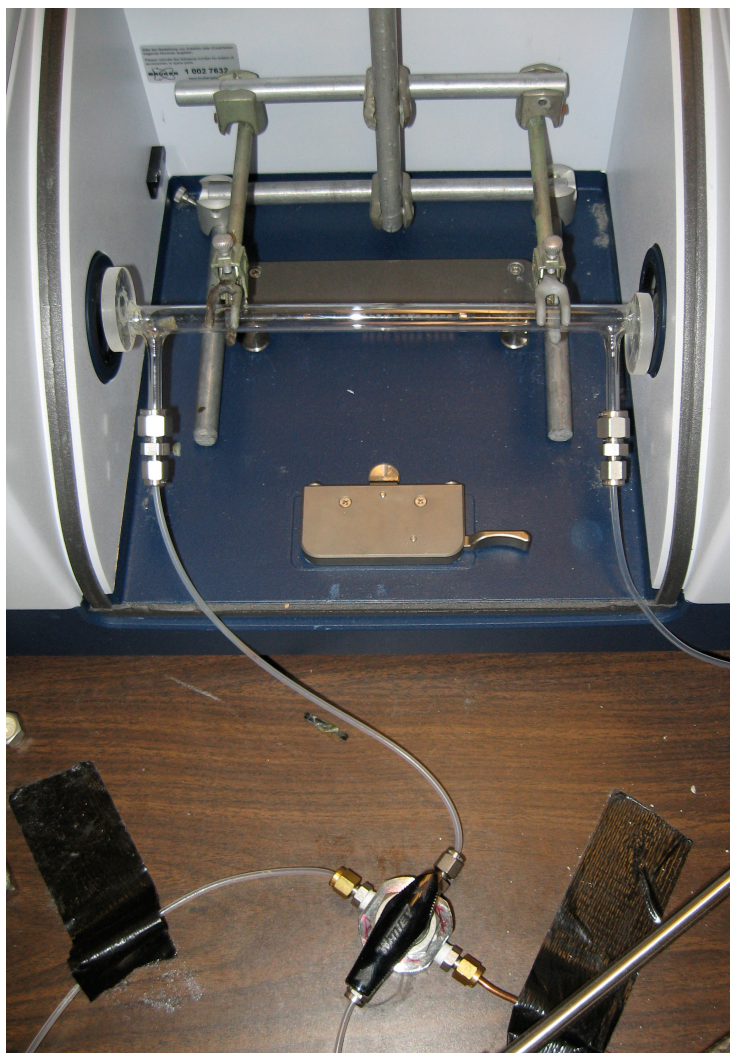
Figure B.1: Photograph of the home-made IR flow cell to be used with a Bruker Optics IR spectrometer.

Each IR spectra was the average of 512 individual spectra recorded at 2cm^{-1} resolution. Before an experiment, a background spectrum is taken using Argon flow through the flow cell. Another background spectrum is taken at the end of the experiment. The two background spectra are used to account for the slightly changing concentration of CO_2 due to temperature, humidity, and indoor environmental variations. In addition to background correction, each experiment was calibrated using a 500ppm CO_2 standard.

APPENDIX C

Matlab Code Used for Spectrum Processing

C.1 Raman Spectrum Analysis Code

The following code was used to analyze Raman specra from data obtained in Chapter 3.

C.1.1 Main Code

```
clc

clear


A=importdata('48hrUV200C/Raman/48hrUV200C_1319.txt');

B=importdata('48hrUV200C/Raman/48hrUV200C_1321.txt');

C=importdata('48hrUV200C/Raman/48hrUV200C_1322.txt');

D=importdata('48hrUV200C/Raman/48hrUV200C_1325.txt');

E=importdata('48hrUV200C/Raman/48hrUV200C_1326.txt');

F=importdata('48hrUV200C/Raman/48hrUV200C_1328.txt');

G=importdata('48hrUV200C/Raman/48hrUV200C_1329.txt');
```

```matlab
H=importdata('48hrUV200C/Raman/48hrUV200C_1330.txt');

I=importdata('48hrUV200C/Raman/48hrUV200C_1332.txt');

J=importdata('48hrUV200C/Raman/48hrUV200C_1333.txt');

K=importdata('48hrUV200C/Raman/48hrUV200C_1334.txt');

L=importdata('48hrUV200C/Raman/48hrUV200C_1336.txt');


x=A.data(:,1);

a=A.data(:,3);

b=B.data(:,3);

c=C.data(:,3);

d=D.data(:,3);

e=E.data(:,3);

f=F.data(:,3);

g=G.data(:,3);

h=H.data(:,3);

i=I.data(:,3);

j=J.data(:,3);

k=K.data(:,3);

l=L.data(:,3);

analysis=[a b c d e f g h i j k l];

TiO2=1;%0=TiO2 sample, 1= TiO2 sample with carbon on it

for ii=1:length(analysis(1,:))

    [r FW y]=malisis(x,analysis(:,ii),TiO2);

    r2(ii)=r;

    TiO2FW(ii)=FW(2,1);

    DbandFW(ii)=FW(2,2);

    VRbandFW(ii)=FW(2,3);
```

```
    VLbandFW(ii)=FW(2,4);

    GRbandFW(ii)=FW(2,5);

    GbandFW(ii)=FW(2,6);

    isfitok=input('Is the fit correct?','s');

    if isfitok=='n'

        ii=ii-1;

    end

%    final(i,:)=[r FW(2,1) FW(2,2) FW(2,3) FW(2,4) FW(2,5) FW(2,6)];

end


Means=[mean(r2) mean(TiO2FW) mean(DbandFW) mean(VRbandFW)

mean(VLbandFW) mean(GRbandFW) mean(GbandFW)]

Stdevs=[std(r2) std(TiO2FW) std(DbandFW) std(VRbandFW)

std(VLbandFW) std(GRbandFW) std(GbandFW)]

% t=[0 12 48];

% plot(t,final)
```

C.1.2   Dependent Functions

The dependent function, 'malisis,' shown above is presented here:

```
function [r FWHMs y] = malisis(x,a,B)

figure

z=zeros(1,length(a));

if B==0

    plot(x,a,x,z,'r')

    xlim([50 250])

    Tbase=input('Add offset to Raw Data from 100-200cm^(-1) ?')

    clf
```

```matlab
    [yC,yT]=TiO2fitting_NoC(x,a+Tbase);

    yT1=yT(x);

    TitaniaA=max(integrate(yT,x,0));

    TiO2values=coeffvalues(yT);

    coefs(2)=TiO2values(2);

    FWHMtio2=TiO2values(3)*(2*log(2))^0.5;

    plot(x,a,x,yT1-Tbase)

    xlim([50 2000])

    Ccoeffs=zeros(1,15);

    carbonA=0;

else

    [y3,y4,y5,y6,y7,y8]=gaussfitter(x,a);

    y=[a-y3(x),a-y4(x),a-y5(x),a-y6(x),a-y7(x),a-y8(x)];

    plot(x,y)

    xlim([50 2000])

    legend('3 functions','4 functions','5 functions','6 functions',
     '7 functions','8 functions')

    clc

    bestfit=input('Best fit? Enter #Gaussian of functions')

    clf

    a=y(:,(bestfit-2));

    plot(x,a,x,z,'r')

    xlim([1000 2000])

    Cbase=input('Add offset to Raw Data from 1300-1600cm^(-1) ?')

    clf

    y1 = carbonpeaks(x,a+Cbase);

    carbonA=max(integrate(y1,x,0));
```

```
    Ccoeffs=coeffvalues(y1);


    plot(x,a,x,z,'r')

    xlim([50 300])

    Tbase=input('Add offset to Raw Data from 100-200cm^(-1) ?')

    clf

    y2 = titaniafitter(x,a+Tbase);

    TitaniaA=max(integrate(y2,x,0));

    coefs=coeffvalues(y2);

    FWHMtio2=coefs(3)*(2*log(2))^0.5;


    plot(x,a,x,y1(x)-Cbase,x,y2(x)-Tbase)

    xlim([50 2000])

end

y=a;


r=carbonA/TitaniaA;

FWHMs=[coefs(2) Ccoeffs(2) Ccoeffs(5) Ccoeffs(8) Ccoeffs(11)

Ccoeffs(14);FWHMtio2 Ccoeffs(3)*sqrt(2*log(2))

Ccoeffs(6)*sqrt(2*log(2)) Ccoeffs(9)*sqrt(2*log(2))

Ccoeffs(12)*sqrt(2*log(2)) Ccoeffs(15)*sqrt(2*log(2))];
```

C.2 Non-linear Regression Code

The following is Matlab code used in Chapter 5.

```
clc

clear
```

```
clf
% close all

rawData=[55.51160032 7.53232E-07
93.19247643 1.38587E-06
170.7097628 1.39779E-06
248.1056623 1.12899E-06
325.6500864 7.1326E-07
364.3009476 5.51204E-07
403.1744227 4.24519E-07
442.0770536 3.31626E-07];

Data=rawData;

R=8.314;
k=0.00008618;
Iphi=7.94e-10;
gamma=1.66e-13;

X1=rawData(:,1);
X1=X1+273;
X2=rawData(:,2)*1e6;%Mol/s
Ea=12.1336;
warning off all
x=0:650;
iter=2;
count=1;
```

```matlab
bw=zeros(4,iter-1);
my_opt=statset('MaxIter',1000,'TolFun', 1e-6);
r2max=0;
for l=1:18
    X2w=rawData(:,2)*1e6;%+rawData(l,3)*1e6*randn(1);
    b=[1e1 .08];%b(1) = k(0)*P(C2H4)*P(O2)*P(H2O), b(2)=Ea,
     b(3)=Egap, b(4)=Np
    ymod=@(b,T) (b(1).*exp(-Ea*1000./(R.*T))).*...
    ...*(1-exp(-(b(2))./(k.*T))).^(l));
    try
        [b,r,J,COVB,mse]=nlinfit(X1,X2w,ymod,b,my_opt);
    catch
        break
    end

    CI=nlparci(b,r,'jacobian',J,'alpha',.682);
    yhat=(b(1).*exp(-Ea*1000./(R.*X1))).*...
    ...*(1-exp(-(b(2))./(k.*X1))).^(l));
    r2=1-(norm(yhat-X2w)/norm(X2w-mean(X2w)))^2;
    if r2>r2max
        r2max=r2;
        bmax=b;
        lmax=l;
        CImax=CI;
    end
end
```

```
b=bmax;

ymod=@(b,T) (b(1).*exp(-Ea*1000./(R.*T))).*...

...*(1-exp(-(b(2))./(k.*T))).^(lmax));

clf

hold on

plot(X1-273,Data(:,2)*1e6,'ko')

xlabel('Temperature (C)')

ylabel('r_{CO_{2}}')

plot(x,ymod(b,x+273))

fprintf(1,'Averaged Data:\nk(0)=\t%f\nEa=\t%f\n

Hbar-omega=\t%d\nNp=\t%f\nR^2=\t%f\n',

b(1),Ea,b(2),lmax,r2)

CImax
```

BIBLIOGRAPHY

BIBLIOGRAPHY

[1] T. A. Westrich, X. Y. Chen, and J. W. Schwank. Isooctane decomposition and carbon deposition over ceria-zirconia supported nickel catalysts. *Applied Catalysis A-General*, 386(1-2):83–93, September 2010.

[2] T.A. Westrich, K.A. Dahlberg, M. Kaviany, and J.W. Schwank. High-temperature photocatalytic ethylene oxidation over TiO_2. *Journal of Physical Chemistry: C*, 2011.

[3] Akira Fujishima, Xintong Zhang, and Donald A. Tryk. TiO_2 photocatalysis and related surface phenomena. *Surface Science Reports*, 63(12):515 – 582, 2008.

[4] Tsutomu Umebayashi, Tetsuya Yamaki, Hisayoshi Itoh, and Keisuke Asai. Analysis of electronic structures of 3d transition metal-doped TiO_2 based on band calculations. *Journal of Physics and Chemistry of Solids*, 63(10):1909 – 1920, 2002.

[5] Meng Ni, Michael K.H. Leung, Dennis Y.C. Leung, and K. Sumathy. A review and recent developments in photocatalytic water-splitting using TiO_2 for hydrogen production. *Renewable and Sustainable Energy Reviews*, 11(3):401 – 425, 2007.

[6] R. Müller and L. Mader. Nanoparticle synthesis at high production rates by flame-spray pryrolysis. *Chemical Engineering Schience*, 58:5111–5119, 2003.

[7] Alexander J. Cowan, Junwang Tang, Wenhua Leng, James R. Durrant, and David R. Klug. Water splitting by nanocrystalline TiO_2 in a complete photo-electrochemical cell exhibits efficiencies limited by charge recombination. *The Journal of Physical Chemistry C*, 114(9):4208–4214, 2010.

[8] M. C. Lee and W. Choi. Solid phase photocatalytic reaction on the soot/TiO_2 interface: The role of migrating OH radicals. *Journal of Physical Chemistry B.*, 106:11818–11822, 2002.

[9] Andrew Mills, Jishun Wang, and Matthew Crow. Photocatalytic oxidation of soot by P25 TiO_2 films. *Chemosphere*, 64(6):1032–1035, August 2006.

[10] R. M. Navarro, M. A. Pena, and J. L. G. Fierro. Hydrogen production reactions from carbon feedstocks: Fossil fuels and biomass. *Chem. Rev.*, 107(10):3952–3991, August 2007.

[11] Shakeel Ahmed, Abdullah Aitani, Faizur Rahman, Ali Al-Dawood, and Fahad Al-Muhaish. Decomposition of hydrocarbons to hydrogen and carbon. *Applied Catalysis A: General*, 359(1-2):1 – 24, 2009.

[12] D. L. Trimm. Onboard fuel conversion for hydrogen-fuel-cell-driven vehicles. *Catalysis Reviews – Science and Engineering*, 43:31–84, 2001.

[13] Praveen K. Cheekatamarla and C.M. Finnerty. Reforming catalysts for hydrogen generation in fuel cell applications. *Journal of Power Sources*, 160(1):490 – 499, 2006.

[14] Eranda Nikolla, Johannes Schwank, and Suljo Linic. Promotion of the long-term stability of reforming Ni catalysts by surface alloying. *Journal of Catalysis*, 250(1):85 – 93, 2007.

[15] Eranda Nikolla, Johannes W. Schwank, and Suljo Linic. Hydrocarbon steam reforming on Ni alloys at solid oxide fuel cell operating conditions. *Catalysis Today*, 136(3-4):243 – 248, 2008.

[16] Dae Hyun Kim, Jong Woo Ryu, Eun Hyung Choi, Gyeong Taek Gong, Hyunjoo Lee, Byung Gwon Lee, and Dong Ju Moon. Production of synthesis gas by autothermal reforming of iso-octane and toluene over metal modified Ni-based catalyst. *Catalysis Today*, 136(3-4):266 – 272, 2008.

[17] Ran Ran, Guoxing Xiong, Shishan Sheng, Weishen Yang, Norbert Stroh, and Herwig Brunner. Catalytic partial oxidation of n-heptane for hydrogen production. *Catalysis Letters*, 88:55–59, 2003.

[18] Sitthiphong Pengpanich, Vissanu Meeyoo, Thirasak Rirksomboon, and Johannes Schwank. Iso-Octane partial oxidation over Ni-Sn/$Ce_{0.75}Zr_{0.25}O_2$ catalysts. *Catalysis Today*, 136(3-4):214 – 221, 2008.

[19] L. Villegas, F. Masset, and N. Guilhaume. Wet impregnation of alumina-washcoated monoliths: Effect of the drying procedure on ni distribution and on autothermal reforming activity. *Applied Catalysis A: General*, 320(0):43 – 55, 2007.

[20] Kazuhisa Murata, Masahiro Saito, Megumu Inaba, and Isao Takahara. Hydrogen production by autothermal reforming of sulfur-containing hydrocarbons over re-modified ni/sr/zro2 catalysts. *Applied Catalysis B: Environmental*, 70(1-4):509 – 514, 2007.

[21] Yazhong Chen, Hengyong Xu, Xianglan Jin, and Guoxing Xiong. Integration of gasoline prereforming into autothermal reforming for hydrogen production. *Catalysis Today*, 116(3):334–340, August 2006.

[22] R.M. Navarro, M.C. Alvarez-Galvan, F. Rosa, and J.L.G. Fierro. Hydrogen production by oxidative reforming of hexadecane over Ni and Pt catalysts supported on Ce/La-doped Al_2O_3. *Applied Catalysis A: General*, 297(1):60 – 72, 2006.

[23] Benjamin D. Gould, Xiaoyin Chen, and Johannes W. Schwank. Dodecane reforming over nickel-based monolith catalysts. *Journal of Catalysis*, 250(2):209–221, September 2007.

[24] M.C. Alvarez-Galvan, R.M. Navarro, F. Rosa, Y. Briceao, F. Gordillo Alvarez, and J.L.G. Fierro. Performance of La,Ce-modified alumina-supported Pt and Ni catalysts for the oxidative reforming of diesel hydrocarbons. *International Journal of Hydrogen Energy*, 33(2):652 – 663, 2008.

[25] Dae Hyun Kim, Jung Shik Kang, Yun Joo Lee, Nam Kuk Park, Young Chul Kim, Suk In Hong, and Dong Ju Moon. Steam reforming of n-hexadecane over noble metal-modified Ni-based catalysts. *Catalysis Today*, 136(3-4):228 – 234, 2008.

[26] T. Setoguchi. Effects if anode material and fuel on anodic reaction of solid oxide fuel cells. *Journal of the Electrochemical Society*, 139:2875–2880, 1992.

[27] S.P. Jiang. A review of anode materials development in sold oxide fuel cells. *Journal of Materials Science*, 39:4405–4439, 2004.

[28] S. McIntosh. Direct hydrocarbon solid oxide fuel cells. *Chemical Reviews*, 104:4845–4866, 2004.

[29] E. Perry Murray, T. Tsai, and S. A. Barnett. A direct-methane fuel cell with a ceria-based anode. *Nature*, 400(6745):649–651, August 1999.

[30] Eranda Nikolla, Johannes Schwank, and Suljo Linic. Comparative study of the kinetics of methane steam reforming on supported Ni and Sn/Ni alloy catalysts: The impact of the formation of Ni alloy on chemistry. *Journal of Catalysis*, 263(2):220 – 227, 2009.

[31] P. Lamp, J. Tachtler, O. Finkenwirth, S. Mukerjee, and S. Shaffer. Development of an auxiliary power unit with solid oxide fuel cells for automotive applications. *Fuel Cells*, 3(3):146–152, 2003.

[32] Erica Perry Murray, Stephen J. Harris, Jiang Liu, and Scott A. Barnett. Direct solid oxide fuel cell operation using isooctane. *Electrochemical and Solid-State Letters*, 9(6):A292–A294, 2006.

[33] Mogens Mogensen and Kent Kammer. Conversion of hydrocarbons in solid oxide fuel cells. *Annual Review of Materials Research*, 33(1):321–331, 2003.

[34] Joon-Ho Koh, Young-Sung Yoo, Jin-Woo Park, and Hee Chun Lim. Carbon deposition and cell performance of Ni-YSZ anode support SOFC with methane fuel. *Solid State Ionics*, 149(3-4):157 – 166, 2002.

[35] M. Flytzani-Stephanopoulos and G. E. Voecks. Autothermal reforming of aliphatic and aromatic hydrocarbon liquids. *International Journal of Hydrogen Energy*, 8(7):539–548, 1983.

[36] J.R. Rostrup-Nielsen. *In Catalysis Science and Technology*. Springer Verlag: New York, 1984.

[37] Jens Rostrup-Nielsen and David L. Trimm. Mechanisms of carbon formation on nickel-containing catalysts. *Journal of Catalysis*, 48(1-3):155 – 165, 1977.

[38] D. L. Trimm. Coke formation and minimisation during steam reforming reactions. *Catalysis Today*, 37(3):233–238, August 1997.

[39] R.T.K. Baker, M.A. Barber, P.S. Harris, F.S. Feates, and R.J. Waite. Nucleation and growth of carbon deposits from the nickel catalyzed decomposition of acetylene. *Journal of Catalysis*, 26(1):51 – 62, 1972.

[40] H. S. Bengaard, J. K. Norskov, J. Sehested, B. S. Clausen, L. P. Nielsen, A. M. Molenbroek, and J. R. Rostrup-Nielsen. Steam reforming and graphite formation on Ni catalysts. *Journal of Catalysis*, 209(2):365–384, July 2002.

[41] Stig Helveg, Carlos Lopez-Cartes, Jens Sehested, Poul L. Hansen, Bjerne S. Clausen, Jens R. Rostrup-Nielsen, Frank Abild-Pedersen, and Jens K. Norskov. Atomic-scale imaging of carbon nanofibre growth. *Nature*, 427(6973):426–429, January 2004.

[42] J. R. Rostrup-Nielsen. Sulfur-passivated nickel catalysts for carbon-free steam reforming of methane. *Journal of Catalysis*, 85(1):31–43, January 1984.

[43] D. L. Trimm. Catalysts for the control of coking during steam reforming. *Catalysis Today*, 49(1-3):3–10, February 1999.

[44] Sittichai Natesakhawat, Rick B. Watson, Xueqin Wang, and Umit S. Ozkan. Deactivation characteristics of lanthanide-promoted sol-gel Ni/Al_2O_3 catalysts in propane steam reforming. *Journal of Catalysis*, 234(2):496 – 508, 2005.

[45] K.O. Christensen, D. Chen, R. Ldeng, and A. Holmen. Effect of supports and ni crystal size on carbon formation and sintering during steam methane reforming. *Applied Catalysis A: General*, 314(1):9 – 22, 2006.

[46] Tadeusz Borowiecki, Andrzej Golebiowski, and Beata Stasinska. Effects of small MoO_3 additions on the properties of nickel catalysts for the steam reforming of hydrocarbons. *Applied Catalysis A: General*, 153(1-2):141–156, May 1997.

[47] Ya-Huei (Cathy) Chin, David L. King, Hyun-Seog Roh, Yong Wang, and Steven M. Heald. Structure and reactivity investigations on supported bimetallic AuNi catalysts used for hydrocarbon steam reforming. *Journal of Catalysis*, 244(2):153–162, December 2006.

[48] Jing Xu and Mark Saeys. Improving the coking resistance of Ni-based catalysts by promotion with subsurface boron. *Journal of Catalysis*, 242(1):217 – 226, 2006.

[49] C.A. Bernardo, I. Alstrup, and J.R. Rostrup-Nielsen. Carbon deposition and methane steam reforming on silica-supported Ni-Cu catalysts. *Journal of Catalysis*, 96(2):517 – 534, 1985.

[50] F. Besenbacher, I. Chorkendorff, B. S. Clausen, B. Hammer, A. M. Molenbroek, J. K. Nrskov, and I. Stensgaard. Design of a surface alloy catalyst for steam reforming. *Science*, 279(5358):1913–1915, 1998.

[51] P. M. Holmblad, J. Hvolbk Larsen, I. Chorkendorff, L. Pleth Nielsen, F. Besenbacher, I. Stensgaard, E. Lgsgaard, P. Kratzer, B. Hammer, and J. K. Nrskov. Designing surface alloys with specific active sites. *Catalysis Letters*, 40:131–135, 1996. 10.1007/BF00815272.

[52] Toshihiko Osaki and Toshiaki Mori. Role of potassium in carbon-free CO_2 reforming of methane on K-promoted Ni/Al_2O_3 catalysts. *Journal of Catalysis*, 204(1):89 – 97, 2001.

[53] Yue-Hua Xu, Da-Hui Liang, Man-Le Liu, and Ding-Zhong Liu. Preparation and characterization of Cu_2O-TiO_2: Efficient photocatalytic degradation of methylene blue. *Materials Research Bulletin*, 43(12):3474 – 3482, 2008.

[54] N. Laosiripojana and S. Assabumrungrat. Methane steam reforming over $Ni/CeZrO_2$ catalyst: Influences of $CeZrO_2$ support on reactivity, resistance toward carbon formation, and intrinsic reaction kinetics. *Applied Catalysis A: General*, 290(1-2):200 – 211, 2005.

[55] Thomas Sperle, De Chen, Rune Ladeng, and Anders Holmen. Pre-reforming of natural gas on a Ni catalyst: Criteria for carbon free operation. *Applied Catalysis A: General*, 282(1-2):195 – 204, 2005.

[56] Sakae Takenaka, Yoshiki Orita, Hiroshi Umebayashi, Hideki Matsune, and Masahiro Kishida. High resistance to carbon deposition of silica-coated Ni catalysts in propane stream reforming. *Applied Catalysis A: General*, 351(2):189 – 194, 2008.

[57] Ilias Gavrielatos, Vasilis Drakopoulos, and Stylianos G. Neophytides. Carbon tolerant Ni-Au SOFC electrodes operating under internal steam reforming conditions. *Journal of Catalysis*, 259(1):75 – 84, 2008.

[58] Ki-Won Jun, Hyun-Seog Roh, and Komandur Chary. Structure and catalytic properties of ceria-based nickel catalysts for CO_2; reforming of methane. *Catalysis Surveys from Asia*, 11:97–113, 2007.

[59] P. Fornasiero, G. Balducci, R. Di Monte, J. Kaspar, V. Sergo, G. Gubitosa, A. Ferrero, and M. Graziani. Modification of the redox behaviour of CeO_2 induced by structural doping with ZrO_2. *Journal of Catalysis*, 164(1):173 – 183, 1996.

[60] Do Kyoung Kim, Klaus Stöwe, Frank Müller, and Wilhelm F. Maier. Mechanistic study of the unusual catalytic properties of a new NiCe mixed oxide for the CO_2 reforming of methane. *Journal of Catalysis*, 247(1):101 – 111, 2007.

[61] Hua Song and Umit S. Ozkan. Ethanol steam reforming over Co-based catalysts: Role of oxygen mobility. *Journal of Catalysis*, 261(1):66 – 74, 2009.

[62] Quan Zhuang, Yongning Qin, and Liu Chang. Promoting effect of cerium oxide in supported nickel catalyst for hydrocarbon steam-reforming. *Applied Catalysis*, 70(1):1–8, 1991.

[63] Tatsuya Takeguchi, Shin nosuke Furukawa, and Masashi Inoue. Hydrogen spillover from NiO to the large surface area CeO2ZrO2 solid solutions and activity of the NiO/CeO2ZrO2 catalysts for partial oxidation of methane. *Journal of Catalysis*, 202(1):14 – 24, 2001.

[64] J.P. Kopasz, D. Applegate, L. Miller, H.K. Liao, and S. Ahmed. Unraveling the maze: Understanding of diesel reforming through the use of simplified fuel blends. *International Journal of Hydrogen Energy*, 30(11):1243 – 1250, 2005.

[65] Alfonso F. Ibarreta and Chih-Jen Sung. Optimization of jet-a fuel reforming for aerospace applications. *International Journal of Hydrogen Energy*, 31(8):1066 – 1078, 2006.

[66] Aidu Qi, Shudong Wang, Guizhi Fu, and Diyong Wu. Autothermal reforming of n-octane on Ru-based catalysts. *Applied Catalysis A: General*, 293(0):71 – 82, 2005.

[67] L. Villegas, N. Guilhaume, H. Provendier, C. Daniel, F. Masset, and C. Mirodatos. A combined thermodynamic/experimental study for the optimisation of hydrogen production by catalytic reforming of isooctane. *Applied Catalysis A: General*, 281(1-2):75 – 83, 2005.

[68] Xiaoyin Chen, Andrew R. Tadd, and Johannes W. Schwank. Carbon deposited on Ni/CeZrO isooctane autothermal reforming catalysts. *Journal of Catalysis*, 251(2):374 – 387, 2007.

[69] B.D. Gould, X. Chen, and J. Schwank. n-Dodecane reforming over Nickel-based monolith catalyts: Deactivation and carbon deposition. *Applied Catalysis A: General*, 334:277–290, 2008.

[70] Xiaoyin Chen, Benjamin D. Gould, and Johannes W. Schwank. n-dodecane reforming over monolith-based Ni catalysts: SEM study of axial carbon distribution profile. *Applied Catalysis A: General*, 356(2):137 – 147, 2009.

[71] Keiichi Tomishige, Takeo Kimura, Jin Nishikawa, Tomohisa Miyazawa, and Kimio Kunimori. Promoting effect of the interaction between Ni and CeO_2 on steam gasification of biomass. *Catalysis Communications*, 8(7):1074 – 1079, 2007.

[72] Jakob J Krummenacher and Lanny D Schmidt. High yields of olefins and hydrogen from decane in short contact time reactors: rhodium versus platinum. *Journal of Catalysis*, 222(2):429 – 438, 2004.

[73] Sangho Yoon, Inyong Kang, and Joongmyeon Bae. Effects of ethylene on carbon formation in diesel autothermal reforming. *International Journal of Hydrogen Energy*, 33(18):4780 – 4788, 2008.

[74] A. Kossiakoff and F.O Rice. Thermal decomposition of hydrocarbons, resonance stabilization and isomerization of free radicals. *J. Am. Chem. Soc.*, 65:590–595, 1943.

[75] J. A. Lercher, R. A. Santen, and H. Vinek. Carbonium ion formation in zeolite catalysis. *Catalysis Letters*, 27:91–96, 1994. 10.1007/BF00806981.

[76] J. Q. Walker and J. B. Maynard. Analysis of vapor-phase pyrolysis products of the four trimethylpentane isomers. *Analytical Chemistry*, 43(12):1548–1557, 1971.

[77] E. Ranzi. Initial product distributions from pyrolysis of normal and branched paraffins. *Ind. Eng. Chem. Fundamen.*, 22:132–139, 1983.

[78] F. Doue and G. Guiochron. Mechanism of pyrolysis of some normal and branched C_6-C_9 alkanes. composition of their pyrolysis products. *J. Phys. Chem.*, 73:2804–2809, 1969.

[79] Koyo Norinaga, Olaf Deutschmann, and Klaus J. Httinger. Analysis of gas phase compounds in chemical vapor deposition of carbon from light hydrocarbons. *Carbon*, 44(9):1790 – 1800, 2006.

[80] E. Ranzi, A. Sogaro, P. Gaffuri, G. Pennati, C.K. Westbrook, and W.J. Pitz. A new comprehensive reaction mechanism for combustion of hydrocarbon fuels. *Combustion and Flame*, 99(2):201 – 211, 1994.

[81] P.v. Zedtwitz and A. Steinfeld. The solar thermal gasification of coal: energy conversion efficiency and CO_2 mitigation potential. *Energy*, 28(5):441 – 456, 2003.

[82] P. V. Zedtwitz and A. Steinfeld. Steam-gasification of coal in a fluidized-bed/packed-bed reactor exposed to concentrated thermal radiation – modeling and experimental validation. *Industrial Engineering Chemical Research*, 44:3852–3861, 2005.

[83] Sunil Dutta Sharma, K.K. Saini, Chander Kant, C.P. Sharma, and S.C. Jain. Photodegradation of dye pollutant under uv light by nano-catalyst doped titania thin films. *Applied Catalysis B: Environmental*, 84(1-2):233 – 240, 2008.

[84] Ammar Houas, Hinda Lachheb, Mohamed Ksibi, Elimame Elaloui, Chantal Guillard, and Jean-Marie Herrmann. Photocatalytic degradation pathway of methylene blue in water. *Applied Catalysis B: Environmental*, 31(2):145 – 157, 2001.

[85] Pio Forzatti and Gianpiero Groppi. Catalytic combustion for the production of energy. *Catalysis Today*, 54(1):165 – 180, 1999.

[86] J.A Moulijn, A.E van Diepen, and F Kapteijn. Catalyst deactivation: is it predictable?: What to do? *Applied Catalysis A: General*, 212(1-2):3 – 16, 2001.

[87] P. Christopher, H. Xin, and S. Linic. Visible-light-enhanced catalytic oxidation reactions on plasmonic silver nanostructures. *Nature Chemistry*, 3:467–472, 2011.

[88] Juan M. Coronado, Michael E. Zorn, Isabel Tejedor-Tejedor, and Marc A. Anderson. Photocatalytic oxidation of ketones in the gas phase over TiO_2 thin films: a kinetic study on the influence of water vapor. *Applied Catalysis B: Environmental*, 43(4):329 – 344, 2003.

[89] C. Hagglund, B. Kasemo, and L. Osterlund. In situ reactivity and FTIR study of the wet and dry photooxidation of propane on anatase TiO_2. *Journal of Physical Chemistry B*, 109:10886–10895, 2005.

[90] Xiaojiang Li, Jun ichiro Hayashi, and Chun-Zhu Li. Volatilisation and catalytic effects of alkali and alkaline earth metallic species during the pyrolysis and gasification of victorian brown coal. part vii. Raman spectroscopic study on the changes in char structure during the catalytic gasification in air. *Fuel*, 85(10-11):1509 – 1517, 2006.

[91] Soo-Keun Lee, Sharon McIntyre, and Andrew Mills. Visible illustration of the direct, lateral and remote photocatalytic destruction of soot by titania. *Journal of Photochemistry and Photobiology A: Chemistry*, 162(1):203 – 206, 2004.

[92] Catherine A. Johnson, John W. Patrick, and K. Mark Thomas. Characterization of coal chars by raman spectroscopy, x-ray diffraction and reflectance measurements. *Fuel*, 65(9):1284–1290, September 1986.

[93] H. Darmstadt, L. Sümmchen, J.-M. Ting, U. Roland, S. Kaliaguine, and C. Roy. Effects of surface treatment on the bulk chemistry and structure of vapor grown carbon fibers. *Carbon*, 35(10-11):1581 – 1585, 1997.

[94] T. van der Meulen, A. Mattson, and L. Österlund. A comparative study of the photocatalytic oxidation of propane on anatase, rutile, and mixed-phase anatase-rutile TiO_2 nanoparticles: Role of surface intermediates. *Journal of Catalysis*, 251(1):131 – 144, 2007.

[95] Joana T. Carneiro, Chieh-Chao Yang, Jacob A. Moulijn, and Guido Mul. The effect of water on the performance of TiO_2 in photocatalytic selective alkane oxidation. *Journal of Catalysis*, 277(2):129 – 133, 2011.

[96] M. Primet, P. Pichat, and M. Mathieu. Infrared study of the surface titanium dioxides. 1. hydroxyl groups. *Journal of Physical Chemistry*, 75:1216–1220, 1971.

[97] M. El-Maazawi, A.N. Finken, A.B. Nair, and V.H. Grassian. Adsorption and photocatalytic oxidation of acetone on TiO_2: An in situ transmission FT-IR study. *Journal of Catalysis*, 191(1):138 – 146, 2000.

[98] L Liao, W Wu, C. Chen, and A. L. J. Linsebigler. Photooxidation of formic acid vs formate and ethanol vs ethoxy on TiO_2 and effect of adsorbed water on the rates of formate and formic acid photooxidation. *Journal of Physical Chemistry B*, 105:7678–7685, 2001.

[99] M. A. Henderson. Acetone chemistry on oxidized and reduced $TiO_2(110)$. *Journal of Physical Chemistry B*, 108:18932–18941, 2004.

[100] L. Zhang, H. Fu, and Y. Zhu. Efficient TiO_2 photocatalysis from surface hybridization of TiO_2 part with graphite-like carbon. *Advanced Functional Materials*, 18:2180–2189, 2008.

[101] Joana T. Carneiro, Tom J. Savenije, Jacob A. Moulijn, and Guido Mul. Toward a physically sound structures: Activity relationship of TiO_2-based photocatalysts. *The Journal of Physical Chemistry C*, 114(1):327–332, 2010.

[102] Fritz J. Knorr, Candy C. Mercado, and Jeanne L. McHale. Trap-state distributions and carrier transport in pure and mixed-phase TiO_2: Influence of contacting solvent and interphasial electron transfer. *The Journal of Physical Chemistry C*, 112(33):12786–12794, 2008.

[103] Hiromitsu Nakajima, Toshiyuki Mori, Qing Shen, and Taro Toyoda. Photoluminescence study of mixtures of anatase and rutile TiO_2 nanoparticles: Influence of charge transfer between the nanoparticles on their photoluminescence excitation bands. *Chemical Physics Letters*, 409(1-3):81 – 84, 2005.

[104] John F. Porter, Yu-Guang Li, and Chak K. Chan. The effect of calcination on the microstructural characteristics and photoreactivity of Degussa P-25 TiO_2. *Journal of Materials Science*, 34:1523–1531, 1999.

[105] Dal-Rung Park, Jinlong Zhang, Keita Ikeue, Hiromi Yamashita, and Masakazu Anpo. Photocatalytic oxidation of ethylene to CO_2 and H_2O on ultrafine powdered TiO_2 photocatalysts in the presence of O_2 and H_2O. *Journal of Catalysis*, 185(1):114 – 119, 1999.

[106] Deanna C. Hurum, Alexander G. Agrios, Kimberly A. Gray, Tijana Rajh, and Marion C. Thurnauer. Explaining the enhanced photocatalytic activity of Degussa P25 mixed-phase TiO_2 using EPR. *The Journal of Physical Chemistry B*, 107(19):4545–4549, 2003.

[107] Wonyong Choi, Andreas Termin, and Michael R. Hoffmann. The role of metal ion dopants in quantum-sized TiO_2: Correlation between photoreactivity and charge carrier recombination dynamics. *The Journal of Physical Chemistry*, 98(51):13669–13679, 1994.

[108] Teruhisa Ohno, Kojiro Tokieda, Suguru Higashida, and Michio Matsumura. Synergism between rutile and anatase TiO_2 particles in photocatalytic oxidation of naphthalene. *Applied Catalysis A: General*, 244(2):383 – 391, 2003.

[109] Tetsuro Kawahara, Yasuhiro Konishi, Hiroaki Tada, Noboru Tohge, Junji Nishii, and Seishiro Ito. A patterned TiO_2(Anatase)/TiO_2(Rutile) bilayer-type photocatalyst: Effect of the anatase/rutile junction on the photocatalytic activity. *Angewandte Chemie*, 114(15):2935–2937, 2002.

[110] Chunying Wu, Yinghong Yue, Xingyi Deng, Weiming Hua, and Zi Gao. Investigation on the synergetic effect between anatase and rutile nanoparticles in gas-phase photocatalytic oxidations. *Catalysis Today*, 93-95:863 – 869, 2004.

[111] Marye Anne. Fox and Maria T. Dulay. Heterogeneous photocatalysis. *Chemical Reviews*, 93(1):341–357, 1993.

[112] Amy L. Linsebigler, Guangquan. Lu, and John T. Yates. Photocatalysis on TiO_2 surfaces: Principles, mechanisms, and selected results. *Chemical Reviews*, 95(3):735–758, 1995.

[113] Andrew Mills and Stephen Le Hunte. An overview of semiconductor photocatalysis. *Journal of Photochemistry and Photobiology A: Chemistry*, 108(1):1 – 35, 1997.

[114] Aaron Wold. Photocatalytic properties of titanium dioxide (TiO_2). *Chemistry of Materials*, 5(3):280–283, 1993.

[115] I. M. Arabatzis, T. Stergiopoulos, M. C. Bernard, D. Labou, S. G. Neophytides, and P. Falaras. Silver-modified titanium dioxide thin films for efficient photodegradation of methyl orange. *Applied Catalysis B: Environmental*, 42(2):187 – 201, 2003.

[116] Kyeong Youl Jung, Seung Bin Park, and Son-Ki Ihm. Linear relationship between the crystallite size and the photoactivity of non-porous titania ranging from nanometer to micrometer size. *Applied Catalysis A: General*, 224(1-2):229 – 237, 2002.

[117] A.J. Maira, K.L. Yeung, C.Y. Lee, P.L. Yue, and C.K. Chan. Size effects in gas-phase photo-oxidation of trichloroethylene using nanometer-sized TiO_2 catalysts. *Journal of Catalysis*, 192(1):185 – 196, 2000.

[118] Yoshihisa Ohko, Kazuhito Hashimoto, and Akira Fujishima. Kinetics of photocatalytic reactions under extremely low-intensity UV illumination on titanium dioxide thin films. *The Journal of Physical Chemistry A*, 101(43):8057–8062, 1997.

[119] Timothy N. Obee and Steve O. Hay. Effects of moisture and temperature on the photooxidation of ethylene on titania. *Environmental Science & Technology*, 31(7):2034–2038, 1997.

[120] Meng Nan Chong, Bo Jin, Christopher W.K. Chow, and Chris Saint. Recent developments in photocatalytic water treatment technology: A review. *Water Research*, 44(10):2997 – 3027, 2010.

[121] Clive T. Brigden, Stephen Poulston, Martyn V. Twigg, Andrew P. Walker, and Anthony J. J. Wilkins. Photo-oxidation of short-chain hydrocarbons over titania. *Applied Catalysis B: Environmental*, 32(1-2):63 – 71, 2001.

[122] A. V. Vorontsov, E. N. Savinov, G. B. Barannik, V. N. Troitsky, and V. N. Parmon. Quantitative studies on the heterogeneous gas-phase photooxidation of CO and simple VOCs by air over TiO_2. *Catalysis Today*, 39(3):207 – 218, 1997. Photocatalysis and Solar Energy Conversion.

[123] Suzuko Yamazaki, Satoru Tanaka, and Hidekazu Tsukamoto. Kinetic studies of oxidation of ethylene over a TiO_2 photocatalyst. *Journal of Photochemistry and Photobiology A: Chemistry*, 121(1):55 – 61, 1999.

[124] Xianzhi Fu, Louis A. Clark, Walter A. Zeltner, and Marc A. Anderson. Effects of reaction temperature and water vapor content on the heterogeneous photocatalytic oxidation of ethylene. *Journal of Photochemistry and Photobiology A: Chemistry*, 97(3):181 – 186, 1996.

[125] T. W. Tibbitts, K. E. Cushman, X. Fu, M. A. Anderson, and R. J. Bula. Factors controlling activity of zirconia-titania for photocatalytic oxidation of ethylene. *Advances in Space Research*, 22(10):1443 – 1451, 1998.

[126] Akawat Sirisuk, Charles G. Hill, and Marc A. Anderson. Photocatalytic degradation of ethylene over thin films of titania supported on glass rings. *Catalysis Today*, 54(1):159 – 164, 1999.

[127] C. J. Howard, T. M. Sabine, and F. Dickson. Structural and thermal parameters for rutile and anatase. *Acta Crystallographica Section B*, 47(4):462–468, Aug 1991.

[128] R. C. Powell. *Physics of Solid-State Laser Materials*. Springer-Verlag New York, Inc., 1998.

[129] M. Kaviany. *Heat Transfer Physics*. Cambridge University Press, 2008.

[130] Bunsho Ohtani, Yoshimasa Ogawa, and Sei-ichi Nishimoto. Photocatalytic activity of amorphous anatase mixture of titanium(iv) oxide particles suspended in aqueous solutions. *The Journal of Physical Chemistry B*, 101(19):3746–3752, 1997.

[131] Daniel Svadlak, Jana Shanelova, Jiri Malek, Luis A. Perez-Maqueda, Jos Manuel Criado, and Takefumi Mitsuhashi. Nanocrystallization of anatase in amorphous TiO_2. *Thermochimica Acta*, 414(2):137 – 143, 2004.

[132] Huaqing Xie, Qinghong Zhang, Tonggeng Xi, Jinchang Wang, and Yan Liu. Thermal analysis on nanosized TiO_2 prepared by hydrolysis. *Thermochimica Acta*, 381(1):45 – 48, 2002.

[133] Tasoltan T. Basiev, Alexei Yu. Dergachev, Yurii V. Orlovskii, and Alexander M. Prokhorov. Multiphonon nonradiative relaxation from high-lying levels of Nd^{3+} ions in flouride and oxide laser materials. *Journal of Luminescence*, 53(1-6):19 – 23, 1992.

[134] C. B. Layne, W. H. Lowdermilk, and M. J. Weber. Multiphonon relaxation of rare-earth ions in oxide glasses. *Phys. Rev. B*, 16(1):10–20, Jul 1977.

[135] J. Kim and M. Kaviany. Multiphonon-absorption barrier-transition cooling in led. *Journal of Applied Physics*, –:Submitted, 2011.

[136] E Shojaee and M R Mohammadizadeh. First-principles elastic and thermal properties of TiO_2 : a phonon approach. *Journal of Physics: Condensed Matter*, 22(1):015401, 2010.

[137] Toshiaki Ohsaka, Fujio Izumi, and Yoshinori Fujiki. Raman spectrum of anatase, TiO_2. *Journal of Raman Spectroscopy*, 7(6):321–324, 1978.

[138] R. Engelman and J. Jortner. The energy gap law for radiationless transitions in large molecules. *Journal of Molecular Physics*, 18:145–164, 1970.

[139] Xiuli Wang, Zhaochi Feng, Jianying Shi, Guoqing Jia, Shuai Shen, Jun Zhou, and Can Li. Trap states and carrier dynamics of TiO_2 studied by photoluminescence spectroscopy under weak excitation condition. *Phys. Chem. Chem. Phys.*, 12:7083–7090, 2010.

[140] F. Thevenet, O. Guaitella, E. Puzenat, C. Guillard, and A. Rousseau. Influence of water vapor on plasma/photocatalytic oxidation efficiency of acetylene. *Applied Catalysis B: Environmental*, 84:813–820, 2008.

[141] G. L. Chiarello, M.H. Aguirre, and E. Selli. Hydrogen production by photocatalytic steam reforming of methanol on noble metal-modified TiO_2. *Journal of Catalysis*, 273:182–190, 2010.

[142] Deanna C. Hurum, Kimberly A. Gray, Tijana Rajh, and Marion C. Thurnauer. Recombination pathways in the Degussa P25 formulation of TiO_2: Surface versus lattice mechanisms. *The Journal of Physical Chemistry B*, 109(2):977–980, 2005.

[143] Tsutomu Hirakawa and P. Kamat. Charge separation and catalytic activity of Ag@TiO_2 core-shell composite clusters under UV-irradiation. *Journal of the American Chemical Society*, 127:3928–3934, 2005.

[144] M. Haruta. Gold as a novel catalyst in the 21st century: preparation, working mechanism and applications. *Gold Bulletin*, 37:27–36, 2004.

[145] Flora Boccuzzi, Anna Chiorino, Maela Manzoli, Ping Lu, Tomoki Akita, Satoshi Ichikawa, and Masatake Haruta. Au/TiO_2 nanosized samples: A catalytic, TEM, and FTIR study of the effect of calcination temperature on the CO oxidation. *Journal of Catalysis*, 202(2):256 – 267, 2001.

[146] G. Bond. Gold-catalysed oxidation of carbon monoxide. *Gold Bulletin*, 33:41–51, 2000.